DIPLOMARABEIT
Master's Thesis

Bone elasticity determination: quasi-static unloading tests, ultrasound, and micromechanics

ausgeführt zum Zwecke der Erlangung des
akademischen Grades eines Diplom-Ingenieurs

unter der Leitung von

Univ.-Prof. Dipl.-Ing. Dr. techn. Christian Hellmich

und

Dipl.-Ing. Krzysztof Wojciech Łuczyński

Inst.Nr.: E202
Institut für Mechanik der Werkstoffe und Strukturen

eingereicht an der Technischen Universität Wien
Fakultät für Bauingenieurwesen

von

Schwaiger Christoph

Matr.Nr.: 07 26 406
Zehenthofgasse 19/28
A – 1190 Wien

Wien, am 19.3.2014

Abstract

Although the Young's modulus is undoubtedly one of the most important mechanical characteristics of bone, its proper determination in the course of quasi-static mechanical tests is still a matter of debate. In order to shed some light onto this issue, the present Master's thesis is concerned with the accurate determination of elastic properties of bovine cortical bone at millimeter-length-scale. To achieve this goal, a set of cylindrical samples with diameters of 7 mm and heights of 12 mm was extracted from an 18-month-old bovine femur. At first, a representative specimen was saturated with distilled water, whereby its weight gain (corresponding to the filling of vascular pores) was constantly measured, and this allowed for computation of the vascular porosity as $\phi_{vas} = 7.9\%$. Subsequently, a set of uniaxial quasi-static unloading experiments with a displacement level of 0.125 mm and a displacement rate of 0.031 mm/s, gave access to the longitudinal macroscopic Young's modulus as $E_{unloading} = 23.2 \pm 1.2$ GPa.

As a next step, extracellular mass densities of 22 bovine tibia samples were taken from [Lees et al., 1979] and entered a multi-step homogenization scheme for bone as a hierarchical transversely isotropic material, as developed in [Morin and Hellmich, 2014]. Numerical evaluation of the latter, while taking into account the vascular porosity from the wetting and weighing test, delivered a full stiffness tensors of bovine cortical bone at the macroscopic level. The Young's modulus derived from this stiffness tensor and amounting to $E_{hiercarchy} = 22.5 \pm 2.1$ GPa, reveals a very good agreement of the unloading tests and the previously extensively validated model. This elucidates unloading as the key feature to retrieve a "true" elastic modulus from a quasi-static test.

Apart from this findings, which were recently submitted to the *Journal of Biomechanics*, a detailed sample characterization as well as comprehensive results of the quasi-static mechanical tests, and a brief outlook to the future are given as conclusion of the thesis.

Zusammenfassung

Obwohl der Elastizitätmodul zweifelsohne zu den bedeutendsten mechanischen Eigenschaften von Knochen zählt, herrscht bemerkenswerte Uneinigkeit, was seine experimentelle Bestimmung betrifft. Als Beitrag zu dieser offenen Frage beschäftigt sich die vorliegende Diplomarbeit mit der exakten Bestimmung der elastischen Eigenschaften von kortikalem Rinderknochen, und zwar auf dem Längenmaßstab einiger Millimeter. Dazu wurden zylindrischen Proben mit einem Durchmesser von 7 mm und einer Höhe von 12 mm aus einem 18 Monate alten Rinderknochen entnommen. Messung der Kinetik der Gewichtszunahme einer 50 Stunden lang getrockneten Probe im Zuge ihrer Re-saturierung in destilliertem Wasser ließ die Identifikation der in der vaskulären Poren aufnehmbaren Flüssigkeitsmasse, und damit der vaskuläre Porosität, zu: $\phi_{vas} = 7.9\%$. Anschließend wurden uniaxiale quasistatische Entlastungversuche an 17 Proben durchgeführt, mit einem Verschiebungsniveau von 0.125 mm und einer Verschiebungsrate von 0.031 mms^{-1}, woraus der axiale makroskopische E-Modul, $E_{unloading} = 23.2 \pm 1.2$ GPa, bestimmt wurde.
Zur Kontrolle dieses E-Moduls wurde ein experimentell validiertes Homogenisierungsschema nach [Morin and Hellmich, 2014] herangezogen. Dazu wurden von [Lees et al., 1979] bestimmte extrazelluläre Massendichten von Rinderknochen als Eingangsgrößen herangezogen, sowie die zuvorgenannte vaskuläre Porosität. Dies ergab einen E-Modul von $E_{hierarchy} = 22.5 \pm 2.1$, der perfekt mit dem Wert $E_{unloading}$ übereinstimmt. Dies verdeutlicht, dass quasi-statische Entlastung einen verlässlichen Zugang zu elastischen Eigenschaften von Knochen eröffnet.
Diesen Ergebnissen wurden beim *Journal of Biomechanics* zur möglichen Publikation eingereicht. Außerdem werden zusätzliche Details zur Probencharakterisierung, als auch detaillierte Ergebnisse an den Entlastungsversuchen und sowie Zukunftsaussichten auf weitere Versuche gezeigt.

Table of contents

1 Introduction

There is a general agreement in the biomedical engineering community that the elastic or Young's modulus of a biological material in general, and of bone in particular, is one of the most important mechanical characteristics, giving deep insight in the behavior of bony structures under specific (physiologic) loading conditions [Turner and Burr, 1993]. Bearing in mind that the elasticity *per se* is inseparably connected with energy storage, it becomes clear that it can be accurately quantified only from the energy that can be *recovered* from a system, and not the one which has been put into it [Salençon, 2001]. Therefore, this Master's Thesis is focused on determination of bovine cortical bone elasticity at millimeter-length-scale from quasi-static unloading experiments, based on the protocol of [Luczynski et al., 2013].

The core of the thesis is a paper (submitted to the *Journal of Biomechanics*), on the aforementioned unloading tests compared with an experimentally validated hierarchical homogenization scheme developed by [Morin and Hellmich, 2014, Fritsch et al., 2009], and based on the results of ultrasonic experiments of Lees [Lees et al., 1979] complemented by the results of performed wetting and weighing test. In addition to the aforementioned compact study on reliable elasticity determination through a physically sound experimental approach, some further experimental data, such as samples' geometry, velocities of ultrasonic signals transmitted through the bony samples, and comprehensive results of the conducted mechanical tests, are also presented.

Finally, a short future outlook on planned quasi-static unloading tests on cortical bone samples of sub-or-single-millimeter-size, is also given.

2 Paper entitled "Unloading is the key to quasi-static determination of bone elasticity: evidence from ultrasound, wetting and weighing tests, as well as from micromechanics theory", submitted to the Journal of Biomechanics

Unloading is the key to quasi-static determination of bone elasticity: evidence from ultrasound, wetting and weighing tests, as well as from micromechanics theory

Christoph Schwaiger[a], Krzysztof W. Luczynski[a], Maria-Ioana Pastrama[a], Claire Morin[b], Christian Hellmich[a,*]

[a] *Institute for Mechanics of Materials and Structures, Vienna University of Technology (TU Wien), Austria*
[b] *Ecole Nationale Supérieure des Mines de Saint-Etienne, CIS-EMSE, CNRS:UMR5307, LGF, F-42023 Saint Etienne, France*

Abstract

While there is general agreement that the Young's modulus of elasticity is one of the most important mechanical characteristics of bone, there is a considerable lack of agreement on how to retrieve this modulus from a stress-strain curve of a quasi-static mechanical test: A variety of used protocols deliver inconsistent results. We here take a rigorous thermodynamical approach, by relating the elastic modulus to that portion of energy stored in the investigated sample, which is recovered in form of efficient mechanical work upon unloading of the sample. In more detail, evaluation of the linear portions of the unloading portions of the stress-strain curves, corresponding to the time span during which a sample is in full contact with the loading platens, gives access to the longitudinal macroscopic Young's modulus as $E_{unloading} = 23.2 \pm 1.2$ GPa. In order to check the relevance of this number, an experimentally validated hierarchical upscaling scheme quantifying how "universal" patterns in bone microstructure and composition govern bone elasticity at different length scales (Fritsch et al., 2009; Morin & Hellmich, 2014), is used to convert the extravascular bone mass density of bovine limb bone into its elasticity. Additional identification of the vascular porosity from weight gain measurements in the course of a saturation test allows

*Christian Hellmich
Email address: christian.hellmich@tuwien.ac.at (Christian Hellmich)

for upscaling to the macroscopic elasticity, corresponding to a Young's modulus of $E_{hierarchy} = 22.5 \pm 2.1$ GPa. The latter is in perfect agreement with the one stemming from the unloading experiments. Conclusively, unloading tests deliver truly elastic properties, while moduli derived from the loading portion of a stress-strain curve contain also information on inelastic, most probably plastic, deformation events.
Keywords: quasi-static unloading tests, elastic modulus, micromechanics, ultrasound

1. Introduction

There is a general agreement in the biomedical engineering community that the elastic or Young's modulus of a biological material in general, and of bone in particular, is one of the most important mechanical characteristics, giving deep insight into the behavior of bony structures under specific loading conditions (Turner & Burr, 1993). While the idea of the Young's modulus somehow relating stresses imposed onto a material sample to the strains they provoke, is common to all the innumerable scientific investigations comprising Young's modulus determination, there is a considerable lack of agreement on how to actually retrieve the Young's modulus from a given stress-strain curve. Namely, in contradiction to what is known from classical engineering materials such as steel, the stress-strain curve of bone samples is never really linear, and hence, there are different suggestions on how to "define" a Young's modulus for this particular situation: some researchers prefer the "slope of the linear portion" of the stress-strain curve (Keller, 1994; Öhman et al., 2011), others the "slope of the stress–strain relationship between 0.2 and 0.4% strain" (López et al., 2014), "the initial tangent modulus and secant modulus" (Novitskaya et al., 2013), "the linear elastic region" of the loading regime (Vale et al., 2013), "the most linear portion" of the loading regime (Vuola et al., 1998), "the steepest portion" of the loading regime (Metsger et al., 1999), "the longest linear portion" of the loading regime (Chu et al., 2002), "the initial linear region" (Charles-Harris

Nomenclature

$\mathbb{C}^u_{exvas}$ stiffness tensor of the undrained extravascular bone matrix

$\mathbb{C}_{cort}$ stiffness tensor of cortical bone

d diameter of cortical bone sample

$\mathbb{D}_{cort}$ compliance tensor of cortical bone

$E_{hierarchy}$ Young's modulus from experimentally validated hierarchical upscaling scheme for elasticity, together with wetting and weighing tests

$E_{loading}$ modulus derived from loading portion of quasi-static mechanical test

$E_{unloading}$ modulus derived from unloading portion of quasi- static mechanical test

$\mathbf{e}_1, \mathbf{e}_2$ base vectors defining transverse material direction of bone

$\mathbf{e}_3$ base vector defining axial material direction of bone

h height of cortical bone sample

$\mathbb{I}$ fourth-order identity tensor

$\mathbb{P}_{cyl}$ fourth-order Hill tensor for cylindrical inclusions

$\Delta m(t)$ amount of water taken in by the sample over time t

Δm_1 mass uptake related to filling of vascular pores

Δm_2 mass uptake related to filling of pores being significantly smaller than the vascular ones

Δu_{m} displacements between piston and actuator of quasi-static mechanical testing machine

Δu_{t} "true" displacements prescribed on bone sample

ϵ normal strain

σ normal stress

τ_1 characteristic filling time of vascular pores

τ_2 characteristic time of (potentially partial) filling time of pores being significantly smaller than the vascular ones

ϕ_{vas} vascular porosity

et al., 2007; Maquet et al., 2004), or "the tangent at the origin" (Charrière et al., 2001) of the aforementioned stress-strain characteristics. All these different approaches deliver different results, and this difference is sometimes related to the great variability of mechanical properties found in bone. Although this might be (partially) true (and then related to the different compositional nature of different bones, such as different mineral and collagen contents, as well as different porosities at different levels of observation), it is fairly probable that the aforementioned different protocols induce several intrinsic errors to the proper measurement of elastic properties. This becomes more evident when we remember the thermodynamical origin of elasticity (Salençon, 2001). The latter is related to that part of energy stored in the material, which is fully recoverable upon unloading, i.e. which the material then provides to perform work on its surroundings. Hence, while all aforementioned protocols deal with the loading portion of a stress-strain curve, it appears much more rigorous to determine an elastic modulus from the unloading curve, which, as a rule, exhibits a steeper slope than the loading curve (Abdel-Wahab et al., 2011; Luczynski et al., 2012, 2013). Accordingly, we here report unloading mechanical tests on bone samples, for retrieving their Young's modulus. However, rather than just adding another protocol to all the aforementioned ones (and one which again is probable to not coincide with any of them), we here wish to provide further evidence that the presented protocol is really related to elasticity. Therefore, we compare unloading-derived Young's moduli to elastic properties derived from a totally different, yet classical technique: transmission ultrasound. The latter has provided deep insight into the elasticity of bone (Ashman & Rho, 1988; Ashman et al., 1984; McCarthy et al., 1990; Lees et al., 1979b). This technique, however, does not deliver Young's modulus (which is related to uniaxial stress states), but a normal component of the elasticity tensor (which is related to uniaxial strain states). As to relate the latter to the former, the 3D elasticity tensor of the investigated material needs to be known, and more than a decade of intensive micromechanical research (Fritsch & Hellmich, 2007; Morin & Hellmich, 2014; Hellmich & Ulm, 2002; Hellmich et al., 2004) has led to a precise and

effective mathematically cast way of predicting this tensor from the material's hierarchical microstructure and composition, as has been experimentally validated through a vast amount of statistically and physically independent, as well as different biomechanical (including ultrasound), biochemical, and biophysical experimental data into a coherent theoretical framework. The latter reflects different types of "universal" patterns found in mineralized tissues, related to mineral-to-collagen dosage ratios (Vuong & Hellmich, 2011), mineral distribution (Hellmich & Ulm, 2003), and mineral precipitation (Morin & Hellmich, 2013). Thus, the extracellular mass density of the herein mechanically tested material can be directly related to the material's composition and microstructure, as to predict its Young's modulus at the extravascular level by means of an ultrasound-validated hierarchical material law. To further upscale to the macroscopic level as "seen" in our newly performed quasi-static unloading tests, information on the tissue-dependent vascular porosity is needed, which we derive from additional wetting tests. If the corresponding, ultrasonics-based elasticity predictions fit well with the results from the quasi-static unloading tests described here, then the latter turn out indeed as a reliable direct access to the elastic modulus of bone. The corresponding check will be described in the remainder of this paper.

2. Materials and Methods

2.1. Sample preparation and vascular porosity determination

Cortical bone samples (n=17) were extracted from an 18-month-old fresh bovine femur, obtained from a local butcher. As a rule, the samples were kept frozen at a temperature of -20 degrees Celsius between all the preparation steps described in the following, and also between the mechanical campaigns described in Section 2.2. This provides conservation of mechanical properties throughout the preparation and characterization process (Fölsch et al., 2011; Nazarian et al., 2009; Linde & Sørensen, 1993). After cleaning the femur from the remaining soft tissue, it was roughly cut with a hand saw. Subsequently, plane-parallel slices

with a thickness of roughly 12 mm were cut orthogonal to the long bone axis, by means of a diamond saw (Isomet, Buehler, USA) under constant distilled water irrigation. The cutting speed was initially restricted to 7 revolutions per minute (rpm), in order to avoid overheating, and was further reduced to 3 rpm at the end of the cutting process, as to prevent breaking out of the cut-off part from the remaining part. Then cylinders were drilled out along the long bone axis, again under constant distilled water irrigation. The samples obtained in this way exhibited a height of 12.46 ± 0.10 mm (mean value ± standard deviation) and a diameter of 7.83 ± 0.02 mm, see Table 1 for further details.

One characteristic sample was preserved for porosity determination, through the following protocol: it was dried in air at room temperature for 50 hours, in order to empty the vascular pores, and at least partially, the lacunar pores as well. Thereafter, the sample was re-wetted over a time span of 6 days, and the mass increase, corresponding to the amount of water absorbed by the sample, was measured by means of a balance (Mettler Toledo PG503-S DeltaRange, Mono Bloc, Switzerland), using the corresponding density accessory kit. The kinetics of the re-wetting process is expected to be governed by the characteristic size of the porosity to be filled: the larger vascular pores are filled more quickly than the smaller lacunar pores. Accordingly, the mass increase with time, $\Delta m(t)$, is represented as a sum of two decaying functions,

$$\Delta m(t) = \Delta m_1[1 - \exp(-t/\tau_1)] + \Delta m_2[1 - \exp(-t/\tau_2)] \tag{1}$$

where t denotes time, Δm_1 and τ_1 denote the mass uptake and the characteristic time related to vascular pores filling, and Δm_2 and τ_2 refer to (potentially partial) filling of pores being significantly smaller than the vascular ones. Thus, Δm_1 can be used to quantify the vascular porosity, through

$$\phi_{vas} = \frac{4\Delta m_1}{\rho_{H2O}\pi d^2 h} \tag{2}$$

with $\rho_{H2O} = 1.0$ g/cm^3 as the mass density of water, and with d and h as the diameter and the height of the tested sample, respectively.

Table 1: Characteristics of cylindrical bone samples: height, diameter, and loading/unloading moduli

sample	h [mm]	d [mm]	$E_{loading}$ [GPa]	$E_{unloading}$ [GPa]
H13	12.47	7.79	24.4	23.1
H15	12.38	7.80	20.6	25.0
H16	12.52	7.84	20.3	22.6
H19	12.55	7.80	18.4	22.5
H20	12.47	7.85	22.5	24.7
H21	12.38	7.82	18.7	24.7
H22	12.49	7.83	18.8	24.1
H23	12.47	7.85	17.4	23.5
H24	12.48	7.83	18.4	21.8
H25	12.46	7.82	23.0	23.9
H26	12.48	7.84	17.4	21.8
H27	12.46	7.83	22.7	22.7
H28	12.42	7.82	22.2	21.9
H29	12.49	7.87	22.6	23.1
H30	12.43	7.85	21.6	21.8
H31	12.53	7.85	24.2	24.7
H32	12.43	7.84	13.8	22.0
mean value	12.47	7.83	20.4	23.2
standard deviation	0.05	0.02	2.9	1.2

2.2. Quasi-static unloading tests

Uniaxial compressive tests were performed on all samples with a displacement rate of 0.063 mm/s, which lies in the range of typical "quasistatic" loading rates for bone and biomaterial testing (Luczynski et al., 2013; Brynk et al., 2011). In more detail, each sample was repeatedly loaded and unloaded in longitudinal direction (along the sample height), with increasing displacement levels of $\Delta u_{\mathrm{m}} = 0.125$ mm, 0.250 mm, and 0.375 mm, respectively. These displacements were recorded, by means of a Messotron LWG XX sensor, between the actuator (i.e. the movable upper load platen) of the servo-hydraulic testing machine (DLFV-250/DZ-10-D, Walter und Bai, Switzerland), and the piston hosting the oil which moves the actuator. In order to convert these displacements into strains applied to the bone samples, the compliance of the testing machine needs to be considered. Therefore, the force-displacement curve of the plane test setup (without any sample) was recorded for the entire force range employed during the actual experiments performed on the bone samples. The respective, force-specific "machine-only" displacements were then subtracted from the "machine-plus-sample" displacements corresponding to the same applied forces. The accordingly corrected, "true" displacement levels amounted to approximately Δu_{t} =0.063 mm, 0.125 mm, and 0.188 mm, respectively; and the "true" displacement rate amounted to approximately 0.031 mm/s. These „true" displacements Δu_{t} were then converted into normal strains $\epsilon = \Delta u_{\mathrm{t}}/h$; and related to normal stresses $\sigma = 4F/(d^2\pi)$.

As motivated in the Introduction, the longitudinal Young's modulus of each sample, $E_{unloading}$, was retrieved from the unloading portion of the recorded stress-strain characteristic. Due to the fact that the loading platens were not exactly parallel to the loaded surfaces of the sample, the aforementioned stress-strain characteristic was non-linear at the end of each unloading cycle, when the load platens were not anymore in full contact with the sample surfaces. In order to separate this nonlinear portion of the unloading regime from its linear portion at higher stress levels (corresponding to full contact between sample surfaces and load platens), this latter portion was identified by means of a sequence

of linear regressions: Starting from the stress maximum, increasingly long arrays of stress-strain-data-points were linearly approximated by means of least square linear fits. Thereby, the initial array comprised ten data points, corresponding to 1×10^{-2} mm of the unloading path, and the following arrays increased by one data point each. In order to identify the most relevant of the respective regression lines (i.e. the one reflecting the best the linear nature of the unloading curve), the standard deviations of the absolute differences in strain, between each of the regression lines and the corresponding actually recorded data points, were compared. This approach is inspired by the fact that, in case of a normal distribution (like a measurement noise in this case), the difference between the median and the mean value of a statistical sample (here the aforementioned absolute strain differences) decreases with this sample's size. Additionally, the standard deviation of a normal distribution decreases with the mean value approaching the median. On the other hand, the standard deviation increases the more the fitted points deviate from a straight line. Consideration of these facts proposes that the regression line for which the minimum value among all standard deviations was recorded, corresponds to the longest possible set of data points still lying on a straight line (indicating full contact between the sample and the loading platens), and therefore the slope of exactly this regression line was recognized as the Young's modulus.

2.3. Ultrasonics-validated hierarchical elasticity of bone

The elastic constants of the elementary mechanical constituents of bone, namely hydroxyapatite, collagen, and water with some non-collageneous organics, and their dosages within the extracellular bone matrix, determine the tissue-dependent elastic properties of the latter, as was quantified by an upscaling scheme based on homogenization theory (Hellmich et al., 2004; Morin & Hellmich, 2014; Fritsch & Hellmich, 2007), and validated through an extensive ultrasound data base (McCarthy et al., 1990; Lees et al., 1979b, 1994a, 1995; Lees, 1982; Lees et al., 1983), in combination with "universal" composition and mineralization rules for bone tissues (Morin & Hellmich, 2013; Morin

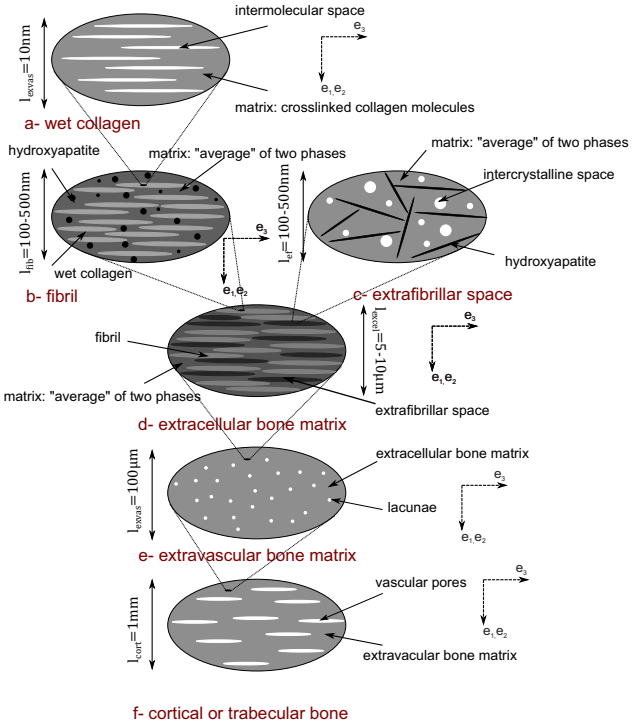

Figure 1: Hierarchical elasticity of cortical bone as represented in a six-scale micromechanical model (Morin & Hellmich, 2014): (a) representative volume element (RVE) of molecular collagen, (b) RVE of mineralized fibril, (c) RVE of extrafibrillar space, (d) RVE of extracellular bone matrix–bone ultrastructure, (e) RVE of extravascular bone matrix, (f) RVE of cortical bone, ($\mathbf{e}_1$, $\mathbf{e}_2$: transverse material directions; $\mathbf{e}_3$: axial material direction); figure illustrates 2D sketches of 3D RVEs

et al., 2013; Vuong & Hellmich, 2011; Hellmich & Ulm, 2003), which were derived from a wealth of biophysical, biochemical, and biomechanical experimental sources (Lees et al., 1979a; Bonar et al., 1985; Prostak & Lees, 1996; Zylberberg et al., 1998; Lees, 2003; Hammet, 1925; Gong et al., 1964; Burns, 1929; Biltz & Pellegrino, 1969; Rougvie & Bear, 1953; Meek et al., 1991; Lees & Mook, 1986; Lees & Heeley, 1981; Lees et al., 1984; Katz & Li, 1973; Hodge & Petruska, 1963; Bergman & Loxley, 1963). Given the aforementioned composition rules, the elastic properties of the extracellular matrix are uniquely linked to the tissue mass densities. For bovine hind limbs, the bone tissue mass density is reported

to amount to 2.044 ± 0.430 g/cc (Lees et al., 1979b). Input of the respective compositional characteristics, into the homogenization steps sketched in Figure 1(a)-(d), in terms of volume fractions of molecular collagen, hydroxyapatite, wet collagen, and fibrils, delivers the extracellular bone matrix stiffness as

$$\mathbb{C}_{excel} = \begin{pmatrix} C_{1111} & C_{1122} & C_{1133} & 0 & 0 & 0 \\ C_{1122} & C_{2222} & C_{2233} & 0 & 0 & 0 \\ C_{1133} & C_{2233} & C_{3333} & 0 & 0 & 0 \\ 0 & 0 & 0 & 2C_{2323} & 0 & 0 \\ 0 & 0 & 0 & 0 & 2C_{1313} & 0 \\ 0 & 0 & 0 & 0 & 0 & 2C_{1212} \end{pmatrix} =$$

$$= \begin{pmatrix} 28.9 \pm 3.4 & 10.8 \pm 0.7 & 12.1 \pm 0.8 & 0 & 0 & 0 \\ 10.8 \pm 0.7 & 28.9 \pm 3.4 & 12.1 \pm 0.8 & 0 & 0 & 0 \\ 12.1 \pm 0.8 & 12.1 \pm 0.8 & 37.3 \pm 3.2 & 0 & 0 & 0 \\ 0 & 0 & 0 & 19.2 \pm 1.8 & 0 & 0 \\ 0 & 0 & 0 & 0 & 19.2 \pm 1.8 & 0 \\ 0 & 0 & 0 & 0 & 0 & 18.1 \pm 1.7 \end{pmatrix} \text{ in GPa} \tag{3}$$

However, we still need to check the relevance of the measurements described in Section 2.2 at the macroscopic (rather than at the extracellular) level. Therefore, we first upscale from the extracellular to the extravascular level, considering undrained lacunar pores with typical volume fraction of 10% (Tai et al., 2008; Morin & Hellmich, 2014), being embedded into extracellular bone matrix

material, see Figure 1(e), yielding the extravascular stiffness as

$$\mathbb{C}^{u}_{exvas} = \begin{pmatrix} 24.2 \pm 1.0 & 9.2 \pm 0.6 & 10.2 \pm 0.6 & 0 & 0 & 0 \\ 9.2 \pm 0.6 & 24.2 \pm 1.0 & 10.2 \pm 0.6 & 0 & 0 & 0 \\ 10.2 \pm 0.6 & 10.2 \pm 0.6 & 30.6 \pm 2.5 & 0 & 0 & 0 \\ 0 & 0 & 0 & 15.8 \pm 1.4 & 0 & 0 \\ 0 & 0 & 0 & 0 & 15.8 \pm 1.4 & 0 \\ 0 & 0 & 0 & 0 & 0 & 14.9 \pm 1.3 \end{pmatrix} \text{ in GPa} \tag{4}$$

Finally, the macroscopic stiffness tensor is computed applying a Mori-Tanaka scheme to a representative volume element (RVE) consisting of a vascular bone matrix (with a volume fraction of $1 - \phi_{vas}$) and of (drained) extra-vascular cylindrical pores (with a volume fraction of ϕ_{vas} and vanishing stiffness), as sketched in Figure 1(f), yielding

$$\mathbb{C}_{macro} = (1 - \phi_{vas})\mathbb{C}^{u}_{exvas} : \{\phi_{vas}[\mathbb{I} + \mathbb{P}_{cyl} : (-\mathbb{C}^{u}_{exvas})]^{-1} + (1 - \phi_{vas})\mathbb{I}\}^{-1} \tag{5}$$

where $\mathbb{I}$ is the fourth-order identity tensor and $\mathbb{P}_{cyl}$ is the fourth-order Hill tensor accounting for the cylindrical shape of the vascular pores being embedded into the transversely isotropic extravascular bone matrix, see (Hellmich et al., 2004). Eq.(5) readily delivers the longitudinal Young's modulus through

$$E_{hierarchy} = \frac{1}{D_{macro,3333}} \tag{6}$$

where $D_{macro,3333}$ is the longitudinal normal component of the macroscopic compliance tensor $\mathbb{D}_{macro}$, which is the inverse of the macroscopic stiffness tensor given through Eq.(5),

$$\mathbb{D}_{macro} = \mathbb{C}^{-1}_{macro} \tag{7}$$

3. Results

All loading and unloading paths recorded during the quasi-static tests exhibit a markedly nonlinear portion at lower stress levels, see Figure 3 for tests

characterized by a maximum displacement level of 0.125 mm. This nonlinear portion reflects incomplete contact between sample surface and load platen, and it is particularly pronounced for tests with a maximum displacement level of 0.063 mm, which were therefore discarded from modulus determination (the latter depending on a linear stress-strain relation). On the other hand, displacement prescription up to a level of 0.188 mm led to frequent (actually almost certain) sample fracture, implying that unloading paths are missing - so that the respective test series could not be used for modulus determination. When applying the analysis described in Section 2.2 to the remaining test series, one obtains a macroscopic Young's modulus of $E_{unloading} = 23.2 \pm 1.2$ GPa. This result needs to be compared to that gained from micromechanical upscaling according to Eq.(4) - (7). This requires knowledge of the vascular porosity, which we gain from evaluation of the drying-wetting test of Section 2.1.

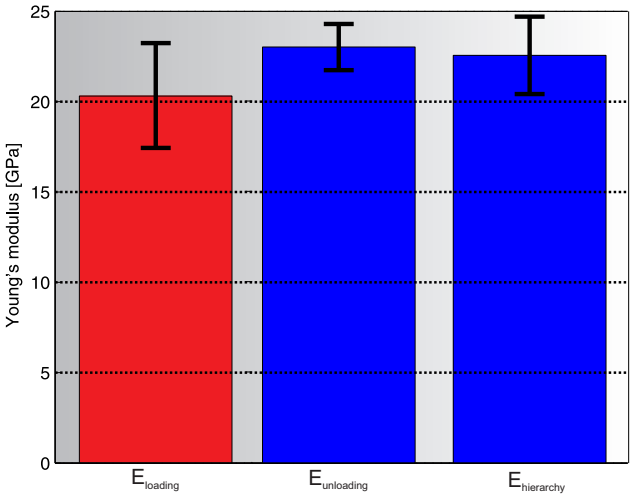

Figure 2: Modulus determination from different sources: from loading and unloading portions of quasi-static mechanical tests ($E_{loading}$ and $E_{unloading}$, respectively), and from hierarchical micromechanical upscaling scheme ($E_{hierarchy}$)

Namely, during the re-wetting test, the sample mass increased by approximately 35 %. Thereby, the rate of water intake decreased over the time span of the experiment, and reached a semi-saturation state characterized by

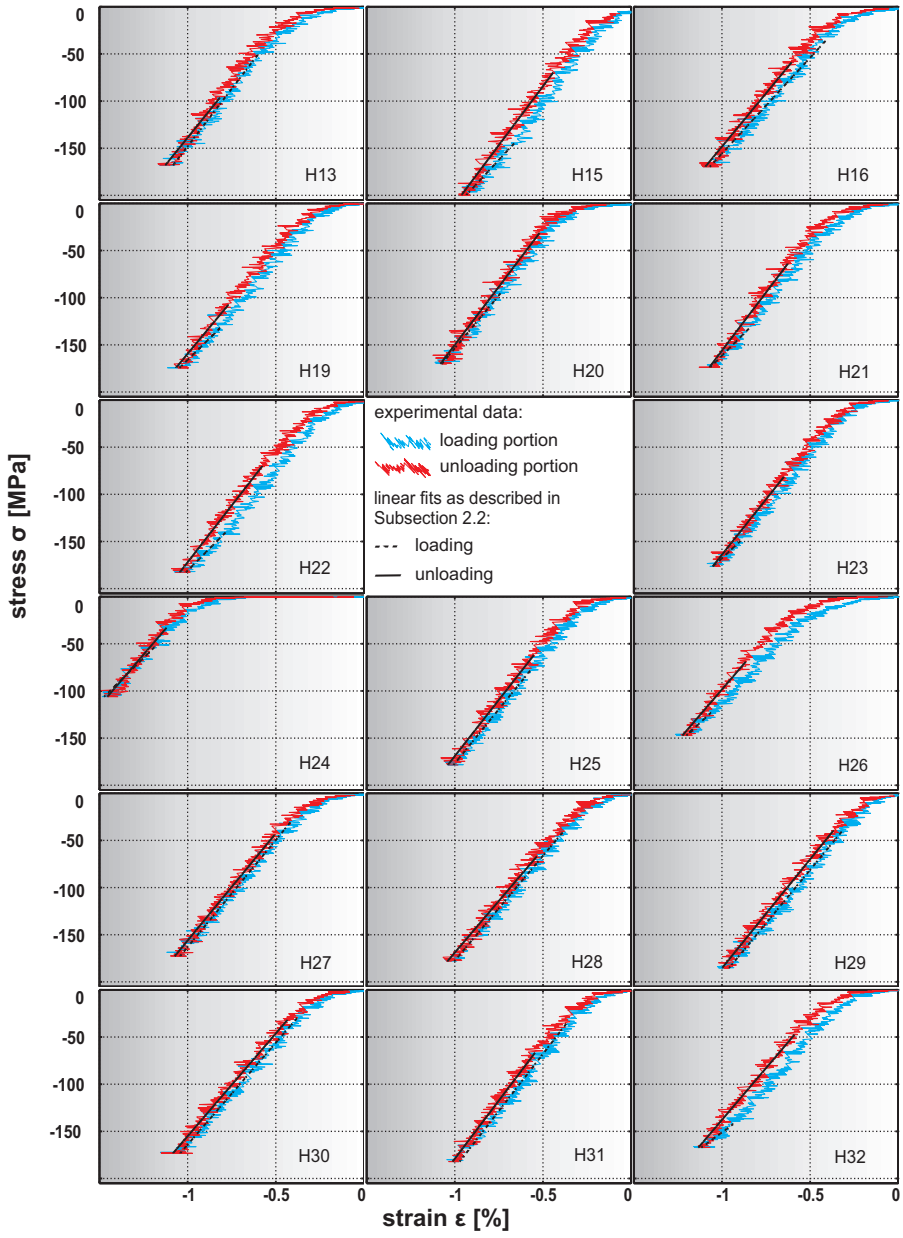

Figure 3: Loading and unloading portions of stress-strain curves gained from quasi-static mechanical tests, characterized by a "true" maximum displacement level of 0.125 mm.

$\Delta m(t = 6\text{d}) = 186.5$ mg. This water intake characteristic was fitted by the bi-exponential function of Eq.(1), with a correlation coefficient of 99 %, see Figure 4; delivering as regression parameters: $\tau_1 = 2.80$ h, $\tau_2 = 28.60$ h, $\Delta m_1 = 42.70$ mg, $\Delta m_2 = 143.78$ mg.

Insertion of the latter value for Δm_1 into Eq.(2) then gives access to the vascular porosity as $\phi_{vas} = 7.9$ %. This value enters the hierarchical micromechanical model as described in Subsection 2.3, which then delivers the full stiffness tensor of the cortical bone according to Eq. (5), see Figure 1(f), reading as

$$\mathbb{C}_{macro}= \begin{pmatrix} 19.1 \pm 1.6 & 7.1 \pm 0.5 & 8.0 \pm 0.5 & 0 & 0 & 0 \\ 7.1 \pm 0.5 & 19.1 \pm 1.6 & 8.0 \pm 0.5 & 0 & 0 & 0 \\ 8.0 \pm 0.5 & 8.0 \pm 0.5 & 27.3 \pm 2.2 & 0 & 0 & 0 \\ 0 & 0 & 0 & 13.5 \pm 1.2 & 0 & 0 \\ 0 & 0 & 0 & 0 & 13.5 \pm 1.2 & 0 \\ 0 & 0 & 0 & 0 & 0 & 12.0 \pm 1.1 \end{pmatrix} \text{ in GPa} \tag{8}$$

The latter gives access to the Young's modulus according to Eq. (6), amounting to $E_{hierarchy} = 22.5 \pm 2.1$ GPa. Finally, for the sake of completeness, a "loading modulus" derived from the loading branches in the same way as the one extracted from the unloading part, was also computed, and amounted to $E_{loading} = 20.4 \pm 2.9$ GPa (see Figure 2 for the comparison of all three moduli).

In order to check whether the loading, unloading, and hierarchical upscaling-derived moduli may still belong to the same statistical population, an analysis of variance (ANOVA) with a significance level of $\alpha = 0.05$ was performed. Thereby, the null hypothesis (stating that pair-wise compared groups of moduli stem from the same population) was rejected for $p < 0.05$. The only pair for which the hypothesis could not have been rejected (the investigated groups then stem from the same population), was the one consisting of the unloading-derived moduli and those stemming from the hierarchical micromechanical upscaling scheme (see Table 2 for the summary of the results and corresponding p-values). This clearly shows that it is an unloading portion of a quasi-static mechanical test,

which delivers an elastic modulus, in contrast to a loading portion.

Table 2: Result of the ANOVA performed on the three groups of moduli; x - null hypothesis can be rejected, ✓- null hypothesis cannot be rejected

	$E_{loading}$	$E_{unloading}$	$E_{hierarchy}$
$E_{loading}$	-	x ($p < 0.01$)	x ($p < 0.02$)
$E_{unloading}$	-	-	✓($p > 0.15$)
$E_{hierarchy}$	-	-	-

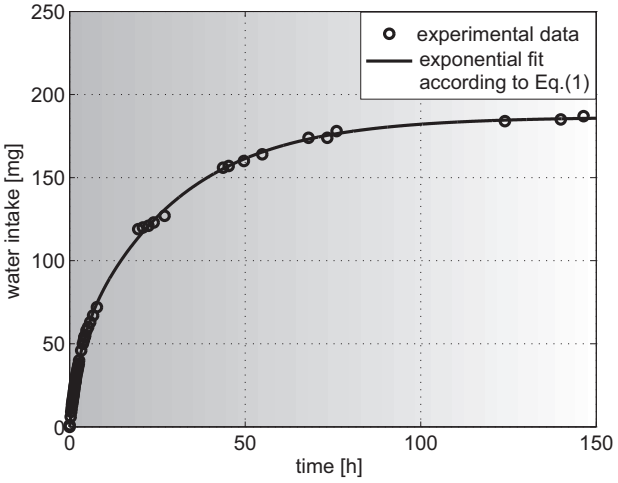

Figure 4: Water intake kinetics of cortical bone sample during re-wetting

4. Discussion

There is a fairly general agreement in the bone mechanics community that bone may exhibit plastic deformation modes, the corresponding discussion going back at least to the 1970's (Burstein et al., 1975). This has been particularly impressively shown in the context of experimental fracture mechanics applied to bone, where a plastic zone around the crack tip, in which elevated stress levels prevail, has been evidenced (Zimmermann et al., 2011; Ritchie et al.,

2009). As regards the nature of these plastic events, the aforementioned authors refer to "fibrillar sliding", a concept also mentioned in the context of mechanical tests with deformation observation through in situ X-ray scattering devices (Gupta et al., 2013). The idea of mutual inelastic displacements between collagen fibrils naturally introduces the role of the *inter*-fibrillar regions, which are more often referred to as extrafibrillar space. The latter hosts the majority of mineral crystals found in bone tissue, as evidenced by microscopic techniques (Lees & Prostak, 1988; Arsenault et al., 1991; Lees et al., 1994b; Prostak & Lees, 1996; Alexander et al., 2012; Benezra Rosen et al., 2002; Jantou et al., 2009; McNally et al., 2013), neutron diffraction (Lees et al., 1984; Bonar et al., 1985; Lees, 1987), and mathematical biology approaches including composite and multiscale mechanics (Hellmich & Ulm, 2003, 2002; Hellmich et al., 2004; Crolet et al., 1993; Aoubiza et al., 1996; Fritsch & Hellmich, 2007; Hamed et al., 2010). The aforementioned nanoscaled mineral crystallites are strongly interacting with the intercrystalline water, as was shown by molecular dynamics simulations (Bhowmik et al., 2007, 2009; Zahn & Hochrein, 2003; Pan et al., 2007). This implies formation of liquid crystal-type interfaces, along which the crystals can glide with respect to each other, in the course of "nanogranular friction between mineral particles", as suggested on the basis of a nanoindentation campaign by (Tai et al., 2006). This nanomechanical origin of bone plasticity was mathematically formulated in terms of a hierarchical elasto-plastic homogenization approach (Fritsch et al., 2009), which predicted amazingly well experimentally determined strength values of bone samples (Currey, 1975; Burstein et al., 1975; Reilly & Burstein, 1974; Currey, 1990), as a function of their composition and porosity. Moreover, it is interesting to note that the aforementioned multiscale elasto-plasticity model for bone proposed elasto-plastic phenomena to occur long before major cracking events may be observed, i.e. even within standard physiological strain levels. It is this proposition which our present experimental campaign has directly confirmed: bone behaves elasto-plastically even at low load levels, and therefore, only the unloading data of quasi-static mechanical experiments deliver truly elastic moduli.

5. Acknowledgement

Financial support within the project MICROBONE (grant number 257023), granted by the ERC is gratefully acknowledged. Moreover, the authors are grateful for the support of Roland Reihsner during the performance of the unloading tests.

6. References

Abdel-Wahab, A. A., Alam, K., & Silberschmidt, V. V. (2011). Analysis of anisotropic viscoelastoplastic properties of cortical bone tissues. *Journal of the Mechanical Behavior of Biomedical Materials*, *4*, 807–820.

Alexander, B., Daulton, T. L., Genin, G. M., Lipner, J., Pasteris, J. D., Wopenka, B., & Thomopoulos, S. (2012). The nanometre-scale physiology of bone: steric modelling and scanning transmission electron microscopy of collagen–mineral structure. *Journal of The Royal Society Interface*, *9*, 1774–1786.

Aoubiza, B., Crolet, J., & Meunier, A. (1996). On the mechanical characterization of compact bone structure using the homogenization theory. *Journal of Biomechanics*, *29*, 1539–1547.

Arsenault, A. L., Frankland, B. W., & Ottensmeyer, F. P. (1991). Vectorial sequence of mineralization in the turkey leg tendon determined by electron microscopic imaging. *Calcified Tissue International*, *48*, 46–55.

Ashman, R., Cowin, S., Van Buskirk, W., & Rice, J. (1984). A continuous wave technique for the measurement of the elastic properties of cortical bone. *Journal of Biomechanics*, *17*, 349–361.

Ashman, R. B., & Rho, J. Y. (1988). Elastic modulus of trabecular bone material. *Journal of Biomechanics*, *21*, 177–181.

Benezra Rosen, V., Hobbs, L., & Spector, M. (2002). The ultrastructure of anorganic bovine bone and selected synthetic hyroxyapatites used as bone graft substitute materials. *Biomaterials*, *23*, 921–928.

Bergman, I., & Loxley, R. (1963). Two improved and simplified methods for the spectrophotometric determination of hydroxyproline. *Analytical Chemistry*, *35*, 1961–1965.

Bhowmik, R., Katti, K. S., & Katti, D. R. (2007). Mechanics of molecular collagen is influenced by hydroxyapatite in natural bone. *Journal of Materials Science*, *42*, 8795–8803.

Bhowmik, R., Katti, K. S., & Katti, D. R. (2009). Mechanisms of load-deformation behavior of molecular collagen in hydroxyapatite-tropocollagen molecular system: steered molecular dynamics study. *Journal of Engineering Mechanics*, *135*, 413–421.

Biltz, R., & Pellegrino, E. (1969). The chemical anatomy of bone. *Journal of Bone and Joint Surgery*, *51-A*, 456–466.

Bonar, L. C., Lees, S., & Mook, H. (1985). Neutron diffraction studies of collagen in fully mineralized bone. *Journal of Molecular Biology*, *181*, 265–270.

Brynk, T., Hellmich, C., Fritsch, A., Zysset, P., & Eberhardsteiner, J. (2011). Experimental poromechanics of trabecular bone strength: Role of Terzaghi's effective stress and of tissue level stress fluctuations. *Journal of Biomechanics*, *44*, 501–508.

Burns, C. (1929). The effect of the continued ingestion of mineral acid on growth of body and bone and on the composition of bone and of the soft tissues. *Biochemical Journal*, *23*, 860–867.

Burstein, A., Zika, J., Heiple, K., & Klein, L. (1975). Contribution of collagen and mineral to the elastic-plastic properties of bone. *Journal of Bone and Joint Surgery*, *57A*, 956 – 961.

Charles-Harris, M., del Valle, S., Hentges, E., Bleuet, P., Lacroix, D., & Planell, J. A. (2007). Mechanical and structural characterisation of completely degradable polylactic acid/calcium phosphate glass scaffolds. *Biomaterials*, *28*, 4429–4438.

Charrière, E., Terrazzoni, S., Pittet, C., Mordasini, P., Dutoit, M., Lemaıtre, J., & Zysset, P. (2001). Mechanical characterization of brushite and hydroxyapatite cements. *Biomaterials*, *22*, 2937–2945.

Chu, T.-M. G., Orton, D. G., Hollister, S. J., Feinberg, S. E., & Halloran, J. W. (2002). Mechanical and in vivo performance of hydroxyapatite implants with controlled architectures. *Biomaterials*, *23*, 1283–1293.

Crolet, J., Aoubiza, B., & Meunier, A. (1993). Compact bone: numerical simulation of mechanical characteristics. *Journal of Biomechanics*, *26*, 677–687.

Currey, J. (1975). The effects of strain rate, reconstruction and mineral content on some mechanical properties of bovine bone. *Journal of Biomechanics*, *8*, 81 – 86.

Currey, J. (1990). Physical characteristics affecting the tensile failure properties of compact bone. *Journal of Biomechanics*, *23*, 837 – 844.

Fölsch, C., Mittelmeier, W., Bilderbeek, U., Timmesfeld, N., von Garrel, T., & Matter, H. P. (2011). Effect of storage temperature on allograft bone. *Transfusion Medicine and Hemotherapy*, *39*, 36–40.

Fritsch, A., & Hellmich, C. (2007). Universal microstructural patterns in cortical and trabecular, extracellular and extravascular bone materials: micromechanics based prediction of anisotropic elasticity. *Journal of Theoretical Biology*, *244*, 597–620.

Fritsch, A., Hellmich, C., & Dormieux, L. (2009). Ductile sliding between mineral crystals followed by rupture of collagen crosslinks: experimentally supported micromechanical explanation of bone strength. *Journal of Theoretical Biology*, *260*, 230–252.

Gong, J., Arnold, J., & Cohn, S. (1964). Composition of trabecular and cortical bone. *The Anatomical Record*, *149*, 325–332.

Gupta, H., Krauss, S., Kerschnitzki, M., Karunaratne, A., Dunlop, J., Barber, A., Boesecke, P., Funari, S., & Fratzl, P. (2013). Intrafibrillar plasticity through mineral/collagen sliding is the dominant mechanism for the extreme toughness of antler bone. *Journal of the Mechanical Behavior of Biomedical Materials*, *28*, 366–382.

Hamed, E., Lee, Y., & Jasiuk, I. (2010). Multiscale modeling of elastic properties of cortical bone. *Acta Mechanica*, *213*, 131–154.

Hammet, F. (1925). A biochemical study of bone growth. I Changes in the ash, organics matter and water during growth (mus norvegicus albinus). *The Journal of Biological Chemistry*, *64*, 409–428.

Hellmich, C., Barthélémy, J.-F., & Dormieux, L. (2004). Mineral–collagen interactions in elasticity of bone ultrastructure–a continuum micromechanics approach. *European Journal of Mechanics-A/Solids*, *23*, 783–810.

Hellmich, C., & Ulm, F.-J. (2002). Micromechanical model for ultrastructural stiffness of mineralized tissues. *Journal of Engineering Mechanics*, *128*, 898–908.

Hellmich, C., & Ulm, F.-J. (2003). Average hydroxyapatite concentration is uniform in the extracollagenous ultrastructure of mineralized tissues: evidence at the 1–10-μm scale. *Biomechanics and Modeling in Mechanobiology*, *2*, 21–36.

Hodge, A., & Petruska, J. (1963). Recent studies with the electron microscope on ordered aggregates of the tropocollagen molecule. In G. Ramachandran (Ed.), *Aspects of Protein Structure – Proceedings of a Symposium held in Madras 14 - 18 January 1963 and organized by the University of Madras, India* (pp. 289 – 300). Academic Press, London and New York.

Jantou, V., Turmaine, M., West, G., Horton, M., & McComb, D. (2009). Focused ion beam milling and ultramicrotomy of mineralised ivory dentine for analytical transmission electron microscopy. *Micron*, *40*, 495–501.

Katz, E., & Li, S. (1973). Structure and function of bone collagen fibrils. *Journal of Molecular Biology*, *80*, 1–15.

Keller, T. S. (1994). Predicting the compressive mechanical behavior of bone. *Journal of Biomechanics*, *27*, 1159–1168.

Lees, S. (1982). Ultrasonic measurements of deer antler, bovine tibia and tympanic bulla. *Journal of Biomechanics*, *15*, 867–874.

Lees, S. (1987). Considerations regarding the structure of the mammalian mineralized osteoid from viewpoint of the generalized packing model. *Connective Tissue Research*, *16*, 281–303.

Lees, S. (2003). Mineralization of type I collagen. *Biophysical Journal*, *85*, 204–207.

Lees, S., Ahern, J., & Leonard, M. (1983). Parameters influencing the sonic velocity in compact calcified tissues of various species. *The Journal of the Acoustical Society of America*, *74*, 28–33.

Lees, S., Bonar, L. C., & Mook, H. A. (1984). A study of dense mineralized tissue by neutron diffraction. *International Journal of Biological Macromolecules*, *6*, 321–326.

Lees, S., Cleary, P. F., Heeley, J. D., & Gariepy, E. L. (1979a). Distribution of sonic plesio-velocity in a compact bone sample. *The Journal of the Acoustical Society of America*, *66*, 641–646.

Lees, S., Hanson, D., & Page, E. A. (1995). Some acoustical properties of the otic bones of a fin whale. *Journal of the Acoustical Society of America*, *99*, 2421–2427.

Lees, S., Hanson, D., Page, E. A., & Mook, H. (1994a). Comparison of dosage-dependent effects of beta-aminopropionitrile, sodium fluoride, and hydrocortisone on selected physical properties of cortical bone. *Journal of Bone and Mineral Research*, *9*, 1377–1389.

Lees, S., & Heeley, J. (1981). Density of a sample bovine cortical bone matrix and its solid constituent in various media. *Calcified Tissue International*, *33*, 499–504.

Lees, S., Heeley, J. D., & Cleary, P. F. (1979b). A study of some properties of a sample of bovine cortical bone using ultrasound. *Calcified Tissue International*, *29*, 107–117.

Lees, S., & Mook, H. (1986). Equatorial diffraction spacing as a function of water content in fully mineralized cow bone determined by neutron diffraction. *Calcified Tissue International*, *39*, 291–292.

Lees, S., & Prostak, K. (1988). The locus of mineral crystallites in bone. *Connective Tissue Researchi*, *18*, 41–54.

Lees, S., Prostak, K., Ingle, V., & Kjoller, K. (1994b). The loci of mineral in turkey leg tendon as seen by atomic force microscope and electron microscopy. *Calcified Tissue Internationali*, *55*, 180–189.

Linde, F., & Sørensen, H. C. F. (1993). The effect of different storage methods on the mechanical properties of trabecular bone. *Journal of Biomechanics*, *26*, 1249–1252.

López, A., Mestres, G., Karlsson Ott, M., Engqvist, H., Ferguson, S. J., Persson, C., & Helgason, B. (2014). Compressive mechanical properties and cytocompatibility of bone-compliant, linoleic acid-modified bone cement in a bovine model. *Journal of the Mechanical Behavior of Biomedical Materials*, *32*.

Luczynski, K., Dejaco, A., Lahayne, O., Jaroszewicz, J., Swieszkowski, W., & Hellmich, C. (2012). Microct/micromechanics-based finite element models

and quasi-static unloading tests deliver consistent values for young's modulus of rapid-prototyped polymer-ceramic tissue engineering scaffold. *Computer Modeling in Engineering & Sciences (CMES)*, *87*, 505–528.

Luczynski, K. W., Brynk, T., Ostrowska, B., Swieszkowski, W., Reihsner, R., & Hellmich, C. (2013). Consistent quasistatic and acoustic elasticity determination of poly-l-lactide-based rapid-prototyped tissue engineering scaffolds. *Journal of Biomedical Materials Research Part A*, *101*, 138–144.

Maquet, V., Boccaccini, A. R., Pravata, L., Notingher, I., & Jérôme, R. (2004). Porous poly (α-hydroxyacid)/bioglass composite scaffolds for bone tissue engineering. i: preparation and in vitro characterisation. *Biomaterials*, *25*, 4185–4194.

McCarthy, R., Jeffcott, L., & McCartney, R. (1990). Ultrasound speed in equine cortical bone: effects of orientation, density, porosity and temperature. *Journal of Biomechanics*, *23*, 1139–1143.

McNally, E., Nan, F., Botton, G. A., & Schwarcz, H. P. (2013). Scanning transmission electron microscopic tomography of cortical bone using z-contrast imaging. *Micron*, *49*, 46–53.

Meek, K., Fullwood, N., Cooke, P., Elliott, G., Maurice, D., Quantock, A., Wall, R., & Worthington, C. (1991). Synchrotron X-ray diffraction studies of the cornea, with implications for stromal hydration. *Biophysical Journal*, *60*, 467–474.

Metsger, D., Rieger, M., & Foreman, D. (1999). Mechanical properties of sintered hydroxyapatite and tricalcium phosphate. *Journal of Materials Science: Materials in Medicine*, *10*, 9–17.

Morin, C., & Hellmich, C. (2013). Mineralization-driven bone tissue evolution follows from fluid-to-solid phase transformations in closed thermodynamic systems. *Journal of Theoretical Biology*, *335*, 185–197.

Morin, C., & Hellmich, C. (2014). A multiscale poromicromechanical approach to wave propagation and attenuation in bone. *Ultrasonics, DOI: 10.1016/j.ultras.2013.12.005*, .

Morin, C., Hellmich, C., & Henits, P. (2013). Fibrillar structure and elasticity of hydrating collagen: A quantitative multiscale approach. *Journal of Theoretical Biology*, *317*, 384–393.

Nazarian, A., Hermannsson, B., Muller, J., Zurakowski, D., & Snyder, B. D. (2009). Effects of tissue preservation on murine bone mechanical properties. *Journal of Biomechanics*, *42*, 82–86.

Novitskaya, E., Lee, S., Lubarda, V. A., & McKittrick, J. (2013). Initial anisotropy in demineralized bovine cortical bone in compressive cyclic loading–unloading. *Materials Science and Engineering: C*, *33*, 817–823.

Öhman, C., Baleani, M., Pani, C., Taddei, F., Alberghini, M., Viceconti, M., & Manfrini, M. (2011). Compressive behaviour of child and adult cortical bone. *Bone*, *49*, 769–776.

Pan, H., Tao, J., Wu, T., & Tang, R. (2007). Molecular simulation of water behaviors on crystal faces of hydroxyapatite. *Frontiers of Chemistry in China*, *2*, 156–163.

Prostak, K., & Lees, S. (1996). Visualization of crystal-matrix structure. in situ demineralization of mineralized turkey leg tendon and bone. *Calcified Tissue International*, *59*, 474–479.

Reilly, D., & Burstein, A. (1974). The elastic modulus for bone. *Journal of Biomechanics*, *7*, 271 – 275.

Ritchie, R. O., Buehler, M. J., & Hansma, P. (2009). Plasticity and toughness in bone. *Physics Today*, *62*, 41–47.

Rougvie, M., & Bear, R. (1953). An X-Ray diffraction investigation of swelling by collagen. *Journal of the American Leather Chemists Association*, *48*, 735–751.

Salençon, J. (2001). *Handbook of continuum mechanics: general concepts-thermoelasticity*. Springer.

Tai, K., Pelled, G., Sheyn, D., Bershteyn, A., Han, L., Kallai, I., Zilberman, Y., Ortiz, C., & Gazit, D. (2008). Nanobiomechanics of repair bone regenerated by genetically modified mesenchymal stem cells. *Tissue Engineering A*, *14*, 1709–1720.

Tai, K., Ulm, F.-J., & Ortiz, C. (2006). Nanogranular origins of the strength of bone. *Nanoletters*, *6*, 2520–2525.

Turner, C. H., & Burr, D. B. (1993). Basic biomechanical measurements of bone: a tutorial. *Bone*, *14*, 595–608.

Vale, A., Pereira, M., Maurício, A., Amaral, P., Rosa, L., Lopes, A., Rodrigues, A., Caetano-Lopes, J., Vidal, B., Monteiro, J., Monteiroe, J., Fonsecab, H., Canhaob, M., & Fatima-Vaza (2013). Micro-computed tomography and compressive characterization of trabecular bone. *Colloids and Surfaces A: Physicochemical and Engineering Aspects*, *438*, 199–205.

Vuola, J., Taurio, R., Göransson, H., & Asko-Seljavaara, S. (1998). Compressive strength of calcium carbonate and hydroxyapatite implants after bone-marrow-induced osteogenesis. *Biomaterials*, *19*, 223–227.

Vuong, J., & Hellmich, C. (2011). Bone fibrillogenesis and mineralization: quantitative analysis and implications for tissue elasticity. *Journal of Theoretical Biology*, *287*, 115–130.

Zahn, D., & Hochrein, O. (2003). Computational study of interfaces between hydroxyapatite and water. *Physical Chemistry Chemical Physics*, *5*, 4004–4007.

Zimmermann, E. A., Schaible, E., Bale, H., Barth, H. D., Tang, S. Y., Reichert, P., Busse, B., Alliston, T., Ager, J. W., & Ritchie, R. O. (2011). Age-related changes in the plasticity and toughness of human cortical bone at multiple

length scales. *Proceedings of the National Academy of Sciences*, *108*, 14416–14421.

Zylberberg, L., Traub, W., de Buffrenil, V., Allizard, F., Arad, T., & Weiner, S. (1998). Rostrum of a toothed whale: Ultrastructural study of a very dense bone. *Bone*, *23*, 241 – 247.

3 Additional activities and future work

In addition to the data described in Section 2, also strength values of some of the tested samples were recorded, see Appendix A for details. Given the success of the protocol described herein, a logical next step consists of applying it to other, particularly lower, length scales. Therefore, a number of sub-or-single-millimeter-sized samples was produced, by realizing another novel protocol: First the bovine femur was cleaned from remaining soft tissue, it was roughly cut with a hand saw into smaller pieces, fitting in the subsequently used diamond saw holder (see Figure 1). Out of these smaller pieces, a few plane-parallel, 2 millimeter-thick slices were

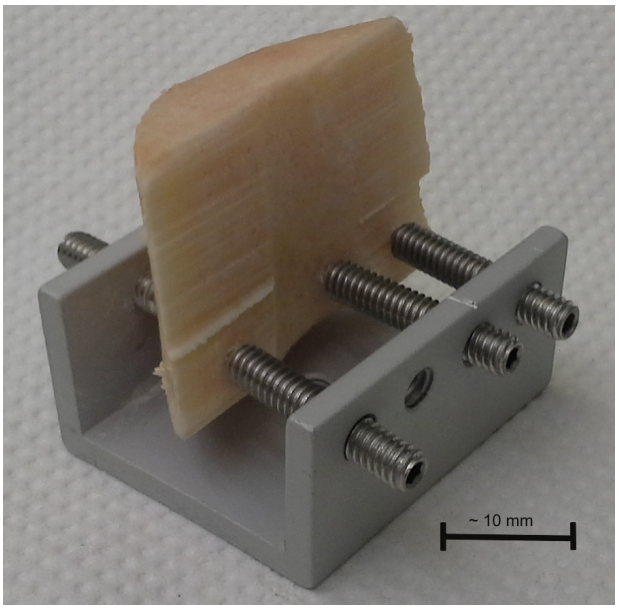

Figure 1: Hard-saw-cut piece of a bovine femur fixed in the diamond saw holder

cut with the aforementioned diamond saw (Isomet, Buehler, USA) under constant distilled water irrigation, in a way that the bottom as well as the top surface of each slice was normal to the long bone axis (see Figure 2). To avoid overheating of the samples a velocity of 7 revolutions per minute (rpm) was chosen, which was then reduced to 3 rpm to prevent breaking out of the cut-off part from the whole sample at the very end of the cutting process. To assure a low surface roughness of cut planes, the saw blade had to be in permanent contact with the sample. Therefore, an appropriate weight was put on the cantilever of the diamond saw. Out of the previously mentioned bony slices, 10 cylinders with 1 mm diameter, and 10 cylinders with a 0.6 mm diameter, were drilled out with a diamond hollow drill (Dr. Müller Diamantmetall AG, Weilheim, Deutschland), see Figure 3. In order to avoid any deviations from the desired cylindrical geometry (occurring at the end of

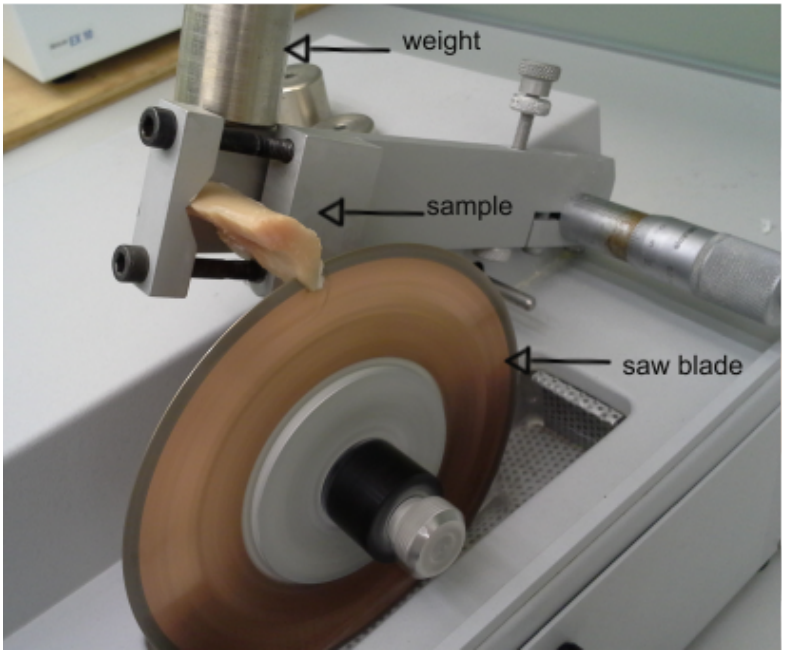

Figure 2: Cutting of bony slices with the diamond saw

the drilling process), a material with a plane surface was put underneath the bone plate, during the drilling. Furthermore, in order to overcome sample heating, a water cooled step-wise drilling method was chosen. The cylindrical samples characterized by the diameter of 0.6 mm had to undergo further preparation steps, because the diameter of the very top differed significantly from the one of the very bottom. To overcome this, each sample was mounted in a hole made in a 1.4 mm thick metal plate in a way that this irregular distal parts were "sticking out" of the metal plate. Subsequently, this "sticking out" parts were polished away with a 800 CAMI sandpaper. Finally, exemplary microscopic images of the resulting samples can be seen in Figure 4.

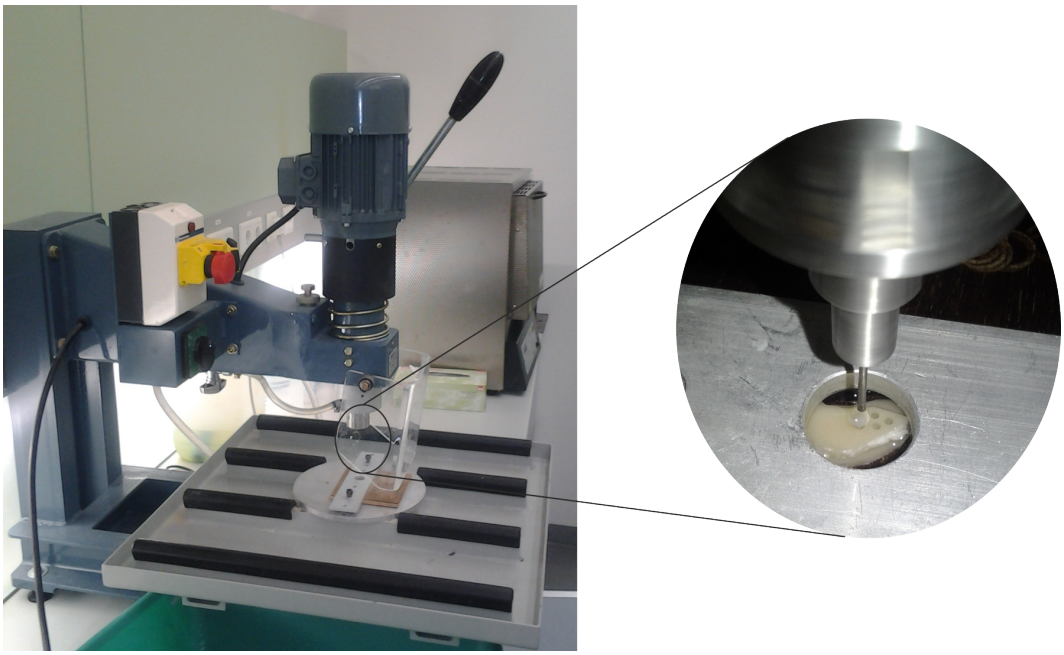

Figure 3: Drilling of cylindrical samples out of a previously cut slice

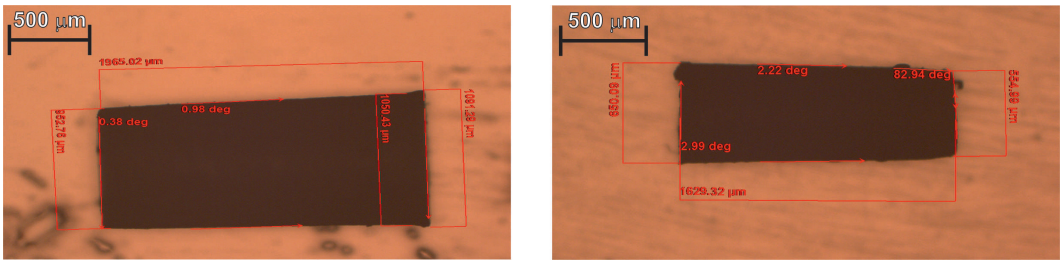

Figure 4: Exemplary light-microscopy images of the millimeter-sized samples

A Appendix I: Sample characterization

Exemplary images of one of the tested samples, as produced and after the destructive test to determine the ultimate stress and strain, can be seen in Fig. 5 and 6, respectively. The ultimate stress was thereby recognized as the maximum force which a sample withstood over its cross-sectional area; the ultimate strain was identified as the corresponding longitudinal displacement (corrected with respect to the complaince of the testing steup as described in Subsection 2.2 in Chapter 2) over the specimen's height. Full sample characterization, including the aforementioned ultimate values, is given in Tables 1,2 and 3. Recorded unloading branches of the stress-strain characteristics with their linear fits (computed as described in Subsection 2.2 of the Chapter 2) as well as ultimate stress and strain values are shown in Fig. (7-27).

Figure 5: Exemplary cortical bone sample: as produced

Figure 6: Exemplary cortical bone sample: after failure

Table 1: Characterization of the H-series samples

name	h [mm][1]	d [mm][2]	E_1 [GPa][3]	E_2 [GPa][4]	σ ult [MPa][5]	ϵ ult [%][6]	v_{1MHz} [m/s][7]	v_{10MHz} [m/s][8]
H12	12.760	7.820	9.185	16.608	125.216	1.552	4080.611	4276.949
H13	12.470	7.790	18.467	23.118	187.014	1.439	4054.262	4207.223
H14	12.860	7.830	15.481	20.545	163.821	1.194	4030.290	4251.966
H15	12.380	7.800	23.264	24.963	213.791	1.252	4023.846	4176.296
H16	12.520	7.840	18.425	22.613	207.754	1.720	4000.851	4239.241
H17	12.680	7.850	-	-	130.590	2.368	3958.220	4264.466
H18	12.670	7.820	-	17.367	188.830	2.005	4050.701	4261.041
H19	12.550	7.800	18.443	22.482	201.561	1.377	3983.282	4264.561
H20	12.470	7.850	19.806	24.671	221.440	1.383	3998.053	4222.000
H21	12.380	7.820	20.324	24.690	204.564	1.435	3927.157	4161.726
H22	12.490	7.830	15.684	24.077	187.781	1.160	3990.881	4243.799
H23	12.470	7.850	19.749	23.503	206.254	1.376	4054.262	4251.861
H24	12.480	7.830	-	21.815	203.600	2.217	3919.765	4181.386
H25	12.460	7.820	20.178	23.878	204.980	1.366	4036.699	4293.930
H26	12.480	7.840	14.517	21.765	169.639	1.605	3933.145	4210.660
H27	12.460	7.830	17.973	22.716	197.722	1.283	3967.194	4218.552
H28	12.420	7.820	18.478	21.923	209.609	1.345	4037.364	4249.526
H29	12.490	7.870	20.720	23.090	200.672	1.228	4018.655	4228.897
H30	12.430	7.850	20.685	21.775	201.848	1.377	3998.581	4253.010
H31	12.530	7.850	20.272	24.689	208.307	1.360	4004.174	4227.842
H32	12.430	7.840	16.440	21.951	171.020	1.311	3984.715	4193.478

Legend:

[1] sample height
[2] sample diameter
[3] Young's modulus derived from the unloading branch stemming from a test with the displacement level of 0.063 mm
[4] Young's modulus derived from the unloading branch stemming from a test with the displacement level of 0.125 mm
[5] ultimate stress
[6] ultimate strain
[7] velocity of the wave transmitted through the sample with a frequency of 1 MHz
[8] velocity of the wave transmitted through the sample with a frequency of 10 MHz

Table 2: Characterization of the J-series samples

name	h [mm][1]	d [mm][2]	E_1 [GPa][3]	E_2 [GPa][4]	σ ult [MPa][5]	ϵ ult [%][6]	v_{1MHz} [m/s][7]	v_{10MHz} [m/s][8]
J1	5.420	3.000	-	-	15.746	0.179	4318.725	4271.080
J2	5.330	3.010	13.280	-	193.949	1.374	4180.392	4372.436
J3	5.300	3.000	12.914	17.460	232.338	1.785	4189.723	4209.690
J4	5.330	2.990	11.915	-	233.240	1.515	4460.251	4301.856
J5	5.250	3.000	6.669	12.596	194.424	1.950	3962.264	4104.769
J6	5.420	2.950	14.218	-	232.629	1.510	4318.725	4339.472
J7	5.400	3.030	11.307	15.481	196.515	1.612	4106.464	4189.294
J8	5.420	3.030	12.556	14.345	260.545	1.958	4153.257	4271.080
J9	5.430	3.040	13.269	-	189.754	1.219	4098.113	4245.504
J10	5.250	2.980	12.827	13.875	254.206	1.571	4320.988	4415.475
J11	5.330	3.000	9.704	11.462	217.059	1.809	3992.509	4103.156
J12	5.320	2.990	10.726	-	227.728	1.461	4108.108	4127.230
J13	5.470	3.070	4.302	12.278	189.806	2.461	3978.182	4243.600
J14	5.380	3.010	9.800	19.514	270.539	1.963	4219.608	4307.446
J15	5.420	3.000	6.769	-	133.690	1.526	3913.357	4172.440
J16	5.450	2.980	10.483	15.040	219.266	1.967	4448.980	4507.858
J17	5.310	2.970	11.133	15.021	222.101	1.744	4197.628	4217.633
J18	5.350	3.000	11.273	12.191	226.538	2.125	4163.424	4182.955
J19	5.490	3.000	10.008	14.101	218.856	1.747	4339.921	4292.416
J20	5.360	3.070	12.434	15.485	206.612	1.727	4203.922	4223.798

Legend:

[1] sample height
[2] sample diameter
[3] Young's modulus derived from the unloading branch stemming from a test with the displacement level of 0.063 mm
[4] Young's modulus derived from the unloading branch stemming from a test with the displacement level of 0.125 mm
[5] ultimate stress
[6] ultimate strain
[7] velocity of the wave transmitted through the sample with a frequency of 1 MHz
[8] velocity of the wave transmitted through the sample with a frequency of 10 MHz

Table 3: Characterization of the K-series samples

name	h [mm][1]	d [mm][2]	E_1 [GPa][3]	E_2 [GPa][4]	σ ult [MPa][5]	ϵ ult [%][6]	v_{1MHz} [m/s][7]	v_{10MHz} [m/s][8]
K1	9.800	4.920	17.303	17.742	206.415	1.460	4041.237	4262.723
K2	9.760	4.910	22.363	22.716	253.416	1.458	4347.439	4418.289
K3	9.690	4.920	16.814	-	233.451	1.413	4240.700	4366.832
K4	9.370	4.900	15.181	19.779	194.035	1.490	4136.865	4261.028
K5	9.630	4.920	18.821	-	222.600	1.371	4347.630	4481.154
K6	9.820	4.920	15.656	22.760	240.800	1.741	4260.304	4425.417
K7	9.950	4.890	11.094	-	89.241	0.959	3879.142	3949.980
K8	9.700	4.910	12.496	18.579	215.126	1.799	4136.461	4293.935
K9	9.700	4.900	18.526	22.948	230.997	1.415	4172.043	4313.028
K10	9.800	4.900	18.760	21.382	232.338	1.357	4233.261	4319.083
K11	9.350	4.970	12.285	21.941	237.989	1.856	4318.707	4433.381
K12	9.790	4.890	13.086	13.342	184.713	2.285	3831.703	3917.567
K13	9.620	4.850	15.837	-	177.883	1.365	4247.241	4374.716
K14	9.770	4.950	8.973	13.553	170.753	2.383	3854.043	4005.740
K15	9.430	4.910	11.194	20.491	199.567	1.661	4145.055	4288.313
K16	9.330	4.900	17.676	19.208	211.572	1.410	4193.258	4204.597
K17	9.820	4.880	8.626	10.998	167.720	1.535	3798.839	3898.372
K18	9.950	4.800	7.838	10.094	95.841	1.715	3894.325	4046.360
K19	9.300	4.850	4.079	19.737	238.150	2.334	4198.646	4229.195
K20	9.940	4.820	7.975	-	115.347	1.627	4167.715	4249.679
K21	9.760	4.840	21.703	23.609	238.085	1.565	4290.110	4378.645

Legend:

[1] sample height
[2] sample diameter
[3] Young's modulus derived from the unloading branch stemming from a test with the displacement level of 0.063 mm
[4] Young's modulus derived from the unloading branch stemming from a test with the displacement level of 0.125 mm
[5] ultimate stress
[6] ultimate strain
[7] velocity of the wave transmitted through the sample with a frequency of 1 MHz
[8] velocity of the wave transmitted through the sample with a frequency of 10 MHz

B Appendix II: Stress-strain curves from quasi-static mechanical tests

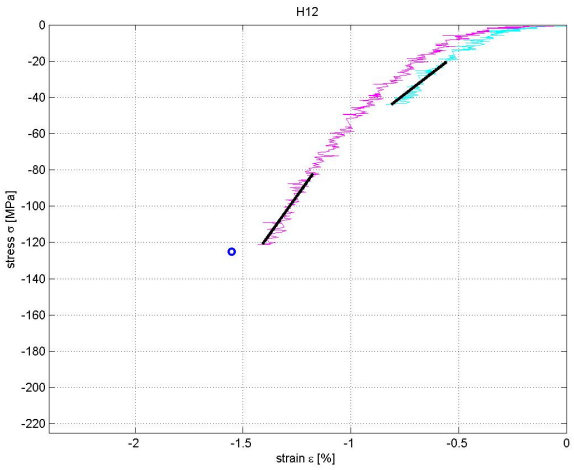

Figure 7: Unloading portions of stress-strain curves obtained from mechanical tests with maximum displacements of 0.063 mm and 0.125 mm, respectively; for the sample with id H12. Black solid lines indicate linear fits computed as described in Subsection 2.2 of the Chapter 2; the blue circle depicts the ultimate stress and strain values

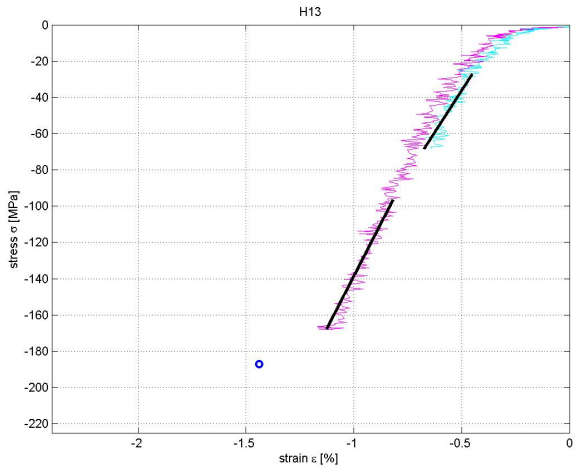

Figure 8: Unloading portions of stress-strain curves obtained from mechanical tests with maximum displacements of 0.063 mm and 0.125 mm, respectively; for the sample with id H13. Black solid lines indicate linear fits computed as described in Subsection 2.2 of the Chapter 2; the blue circle depicts the ultimate stress and strain values

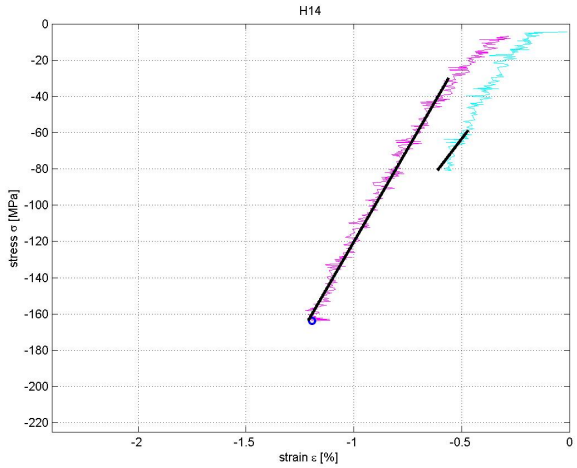

Figure 9: Unloading portions of stress-strain curves obtained from mechanical tests with maximum displacements of 0.063 mm and 0.125 mm, respectively; for the sample with id H14. Black solid lines indicate linear fits computed as described in Subsection 2.2 of the Chapter 2; the blue circle depicts the ultimate stress and strain values

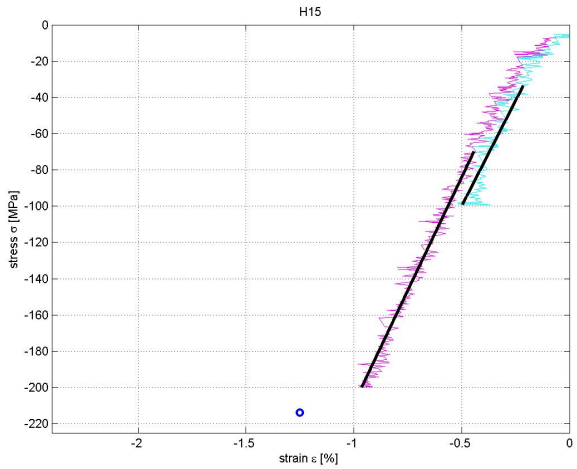

Figure 10: Unloading portions of stress-strain curves obtained from mechanical tests with maximum displacements of 0.063 mm and 0.125 mm, respectively; for the sample with id H15. Black solid lines indicate linear fits computed as described in Subsection 2.2 of the Chapter 2; the blue circle depicts the ultimate stress and strain values

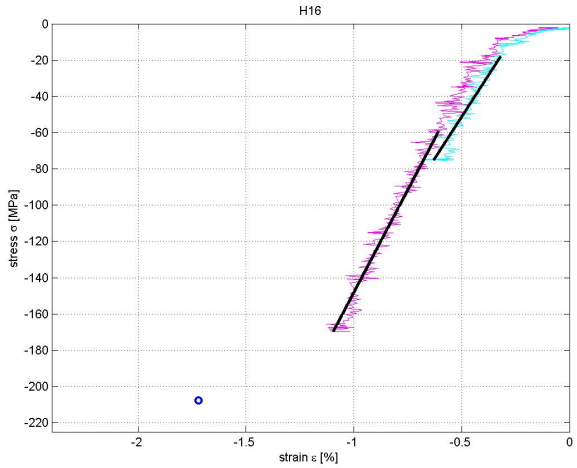

Figure 11: Unloading portions of stress-strain curves obtained from mechanical tests with maximum displacements of 0.063 mm and 0.125 mm, respectively; for the sample with id H16. Black solid lines indicate linear fits computed as described in Subsection 2.2 of the Chapter 2; the blue circle depicts the ultimate stress and strain values

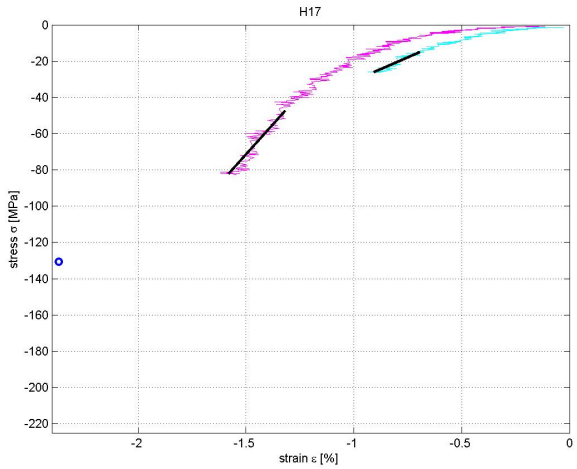

Figure 12: Unloading portions of stress-strain curves obtained from mechanical tests with maximum displacements of 0.063 mm and 0.125 mm, respectively; for the sample with id H17. Black solid lines indicate linear fits computed as described in Subsection 2.2 of the Chapter 2; the blue circle depicts the ultimate stress and strain values

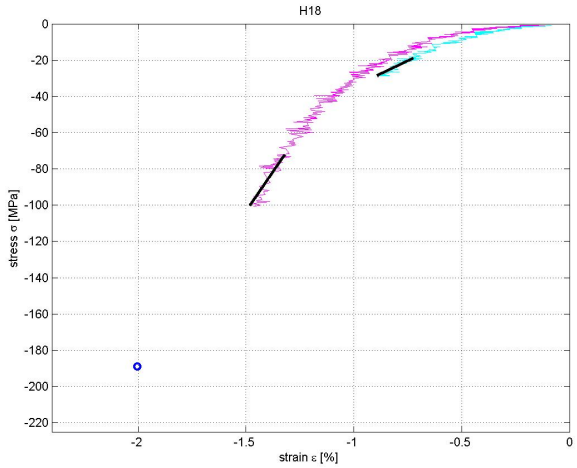

Figure 13: Unloading portions of stress-strain curves obtained from mechanical tests with maximum displacements of 0.063 mm and 0.125 mm, respectively; for the sample with id H18. Black solid lines indicate linear fits computed as described in Subsection 2.2 of the Chapter 2; the blue circle depicts the ultimate stress and strain values

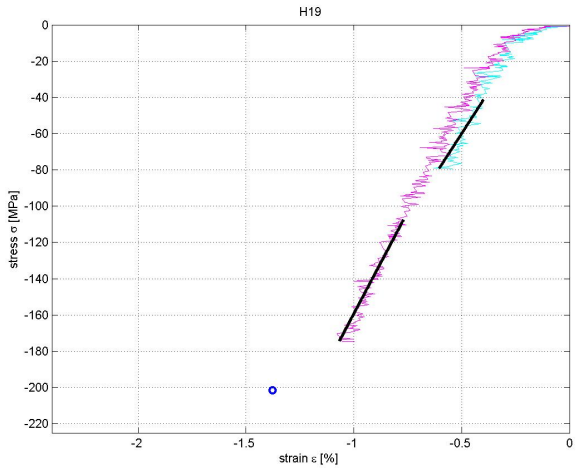

Figure 14: Unloading portions of stress-strain curves obtained from mechanical tests with maximum displacements of 0.063 mm and 0.125 mm, respectively; for the sample with id H19. Black solid lines indicate linear fits computed as described in Subsection 2.2 of the Chapter 2; the blue circle depicts the ultimate stress and strain values

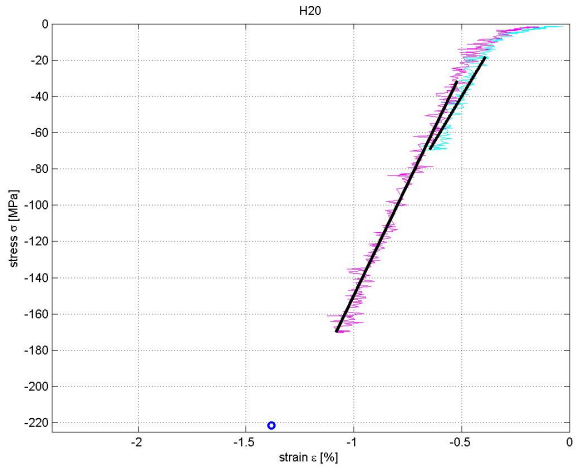

Figure 15: Unloading portions of stress-strain curves obtained from mechanical tests with maximum displacements of 0.063 mm and 0.125 mm, respectively; for the sample with id H20. Black solid lines indicate linear fits computed as described in Subsection 2.2 of the Chapter 2; the blue circle depicts the ultimate stress and strain values

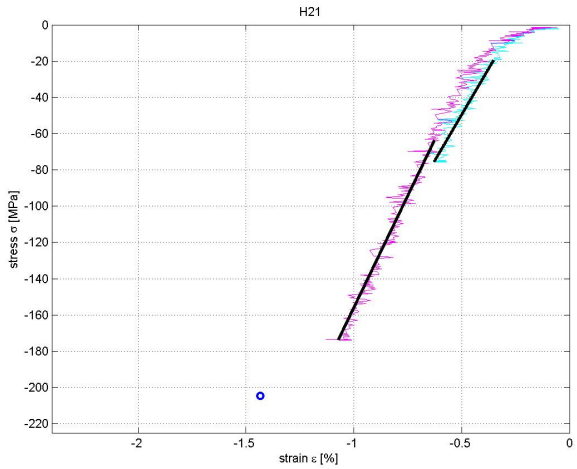

Figure 16: Unloading portions of stress-strain curves obtained from mechanical tests with maximum displacements of 0.063 mm and 0.125 mm, respectively; for the sample with id H21. Black solid lines indicate linear fits computed as described in Subsection 2.2 of the Chapter 2; the blue circle depicts the ultimate stress and strain values

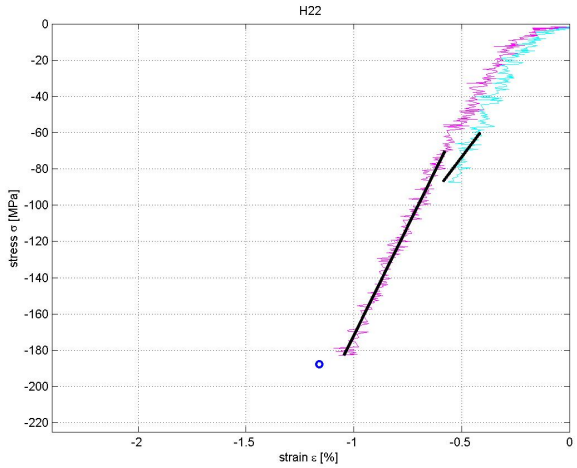

Figure 17: Unloading portions of stress-strain curves obtained from mechanical tests with maximum displacements of 0.063 mm and 0.125 mm, respectively; for the sample with id H22. Black solid lines indicate linear fits computed as described in Subsection 2.2 of the Chapter 2; the blue circle depicts the ultimate stress and strain values

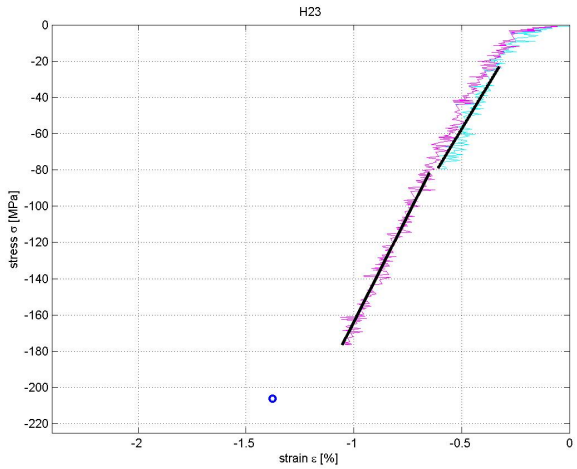

Figure 18: Unloading portions of stress-strain curves obtained from mechanical tests with maximum displacements of 0.063 mm and 0.125 mm, respectively; for the sample with id H23. Black solid lines indicate linear fits computed as described in Subsection 2.2 of the Chapter 2; the blue circle depicts the ultimate stress and strain values

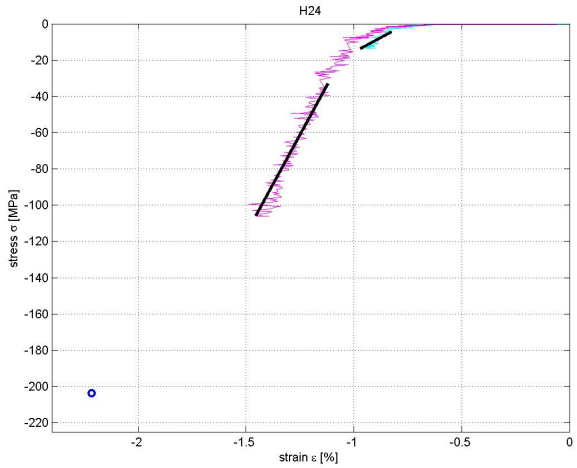

Figure 19: Unloading portions of stress-strain curves obtained from mechanical tests with maximum displacements of 0.063 mm and 0.125 mm, respectively; for the sample with id H24. Black solid lines indicate linear fits computed as described in Subsection 2.2 of the Chapter 2; the blue circle depicts the ultimate stress and strain values

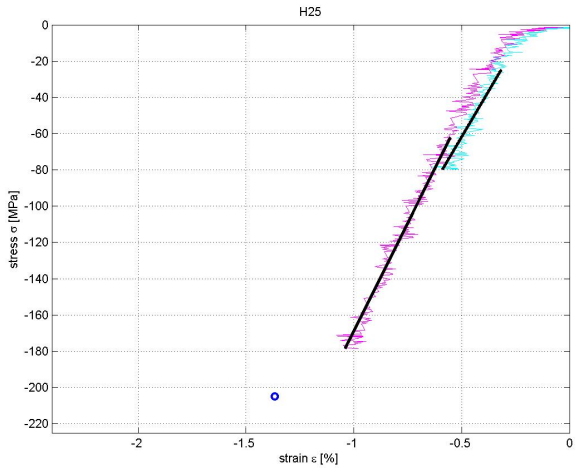

Figure 20: Unloading portions of stress-strain curves obtained from mechanical tests with maximum displacements of 0.063 mm and 0.125 mm, respectively; for the sample with id H25. Black solid lines indicate linear fits computed as described in Subsection 2.2 of the Chapter 2; the blue circle depicts the ultimate stress and strain values

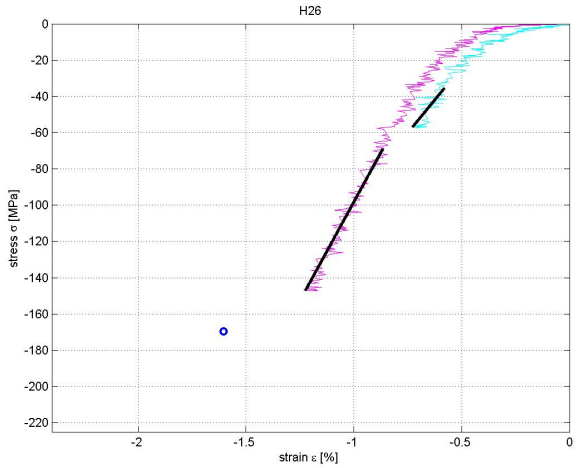

Figure 21: Unloading portions of stress-strain curves obtained from mechanical tests with maximum displacements of 0.063 mm and 0.125 mm, respectively; for the sample with id H26. Black solid lines indicate linear fits computed as described in Subsection 2.2 of the Chapter 2; the blue circle depicts the ultimate stress and strain values

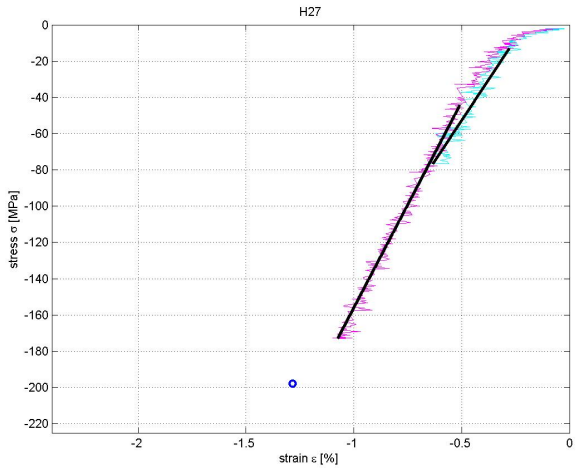

Figure 22: Unloading portions of stress-strain curves obtained from mechanical tests with maximum displacements of 0.063 mm and 0.125 mm, respectively; for the sample with id H27. Black solid lines indicate linear fits computed as described in Subsection 2.2 of the Chapter 2; the blue circle depicts the ultimate stress and strain values

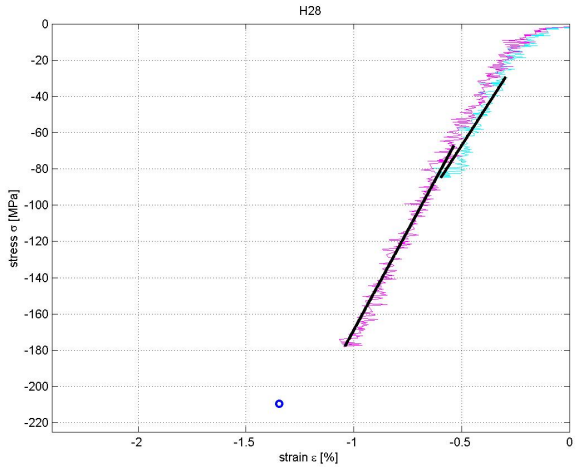

Figure 23: Unloading portions of stress-strain curves obtained from mechanical tests with maximum displacements of 0.063 mm and 0.125 mm, respectively; for the sample with id H28. Black solid lines indicate linear fits computed as described in Subsection 2.2 of the Chapter 2; the blue circle depicts the ultimate stress and strain values

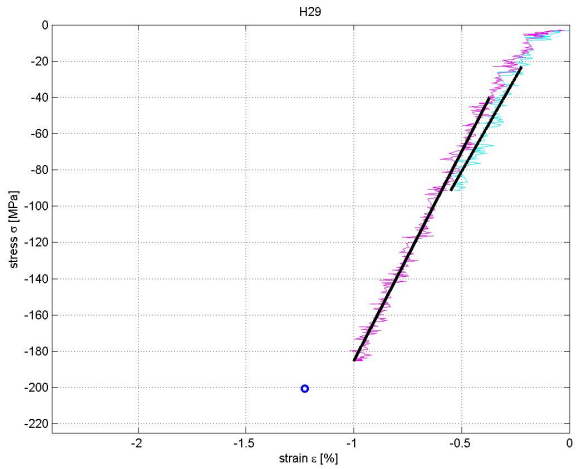

Figure 24: Unloading portions of stress-strain curves obtained from mechanical tests with maximum displacements of 0.063 mm and 0.125 mm, respectively; for the sample with id H29. Black solid lines indicate linear fits computed as described in Subsection 2.2 of the Chapter 2; the blue circle depicts the ultimate stress and strain values

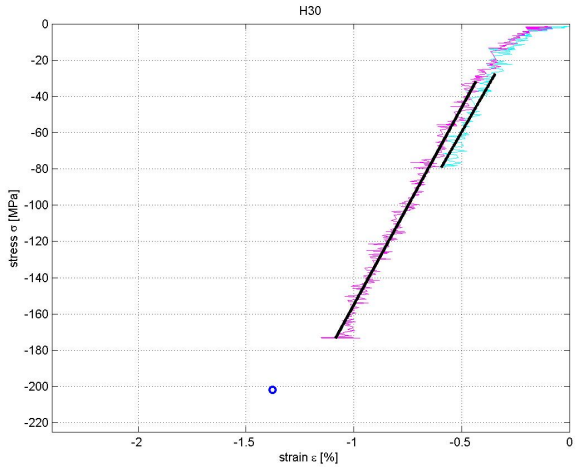

Figure 25: Unloading portions of stress-strain curves obtained from mechanical tests with maximum displacements of 0.063 mm and 0.125 mm, respectively; for the sample with id H30. Black solid lines indicate linear fits computed as described in Subsection 2.2 of the Chapter 2; the blue circle depicts the ultimate stress and strain values

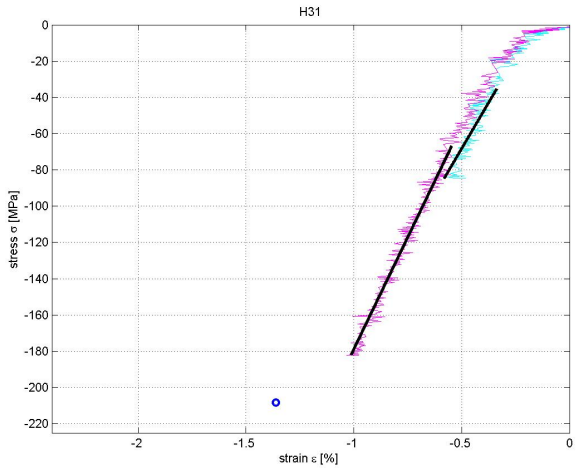

Figure 26: Unloading portions of stress-strain curves obtained from mechanical tests with maximum displacements of 0.063 mm and 0.125 mm, respectively; for the sample with id H31. Black solid lines indicate linear fits computed as described in Subsection 2.2 of the Chapter 2; the blue circle depicts the ultimate stress and strain values

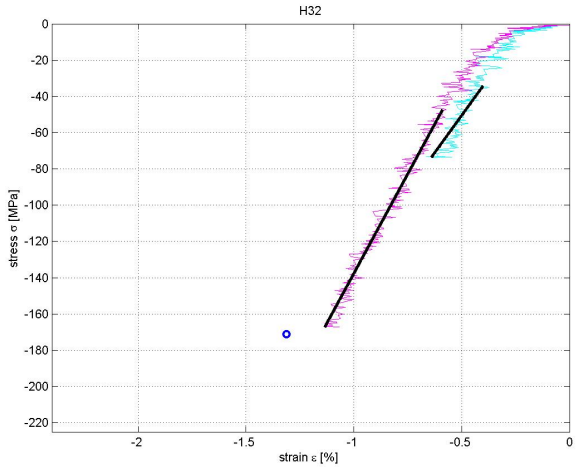

Figure 27: Unloading portions of stress-strain curves obtained from mechanical tests with maximum displacements of 0.063 mm and 0.125 mm, respectively; for the sample with id H32. Black solid lines indicate linear fits computed as described in Subsection 2.2 of the Chapter 2; the blue circle depicts the ultimate stress and strain values

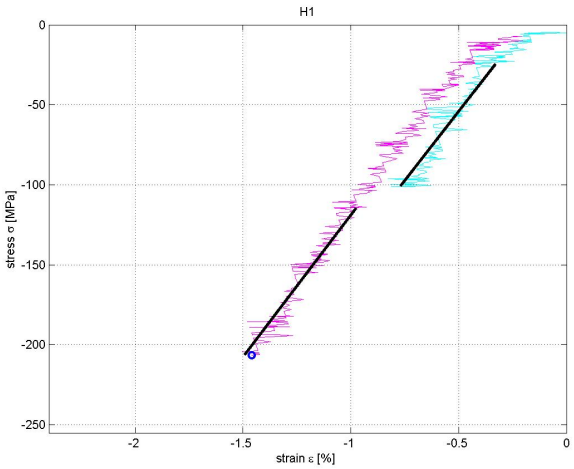

Figure 28: Unloading branches of a stress-strain characteristics stemming from mechanical tests, with a final displacements of 0.048 mm and 0.097 mm for the sample with id K1. Black solid lines indicate linear fits computed as described in subsection 2.2 of the Chapter 2; the blue circle depicts the ultimate stress and strain values

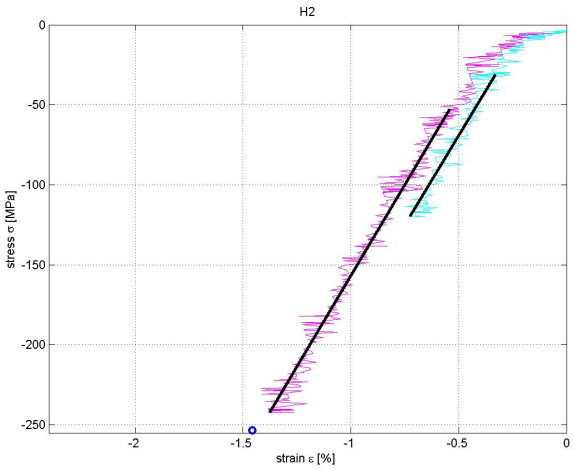

Figure 29: Unloading portions of stress-strain curves obtained from mechanical tests with maximum displacements of 0.048 mm and 0.097 mm for the sample with id K2. Black solid lines indicate linear fits computed as described in Subsection 2.2 of the Chapter 2; the blue circle depicts the ultimate stress and strain values

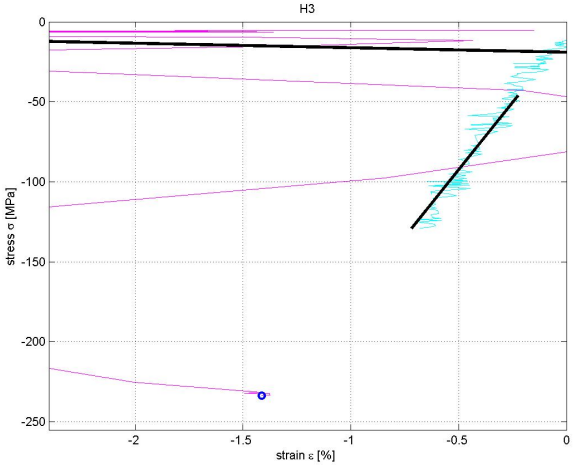

Figure 30: Unloading portions of stress-strain curves obtained from mechanical tests with maximum displacements of 0.048 mm and 0.097 mm for the sample with id K3. Black solid lines indicate linear fits computed as described in Subsection 2.2 of the Chapter 2; the blue circle depicts the ultimate stress and strain values

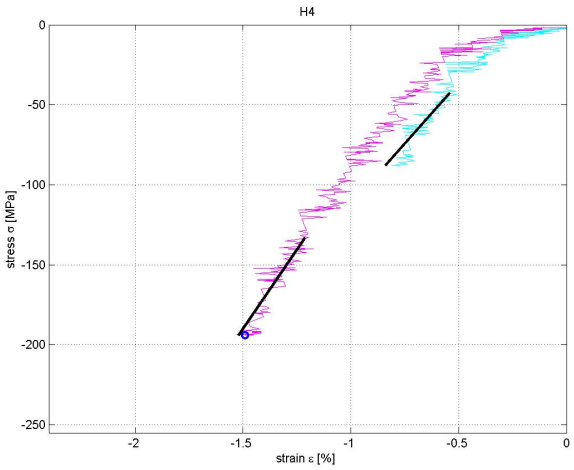

Figure 31: Unloading portions of stress-strain curves obtained from mechanical tests with maximum displacements of 0.048 mm and 0.097 mm for the sample with id K4. Black solid lines indicate linear fits computed as described in Subsection 2.2 of the Chapter 2; the blue circle depicts the ultimate stress and strain values

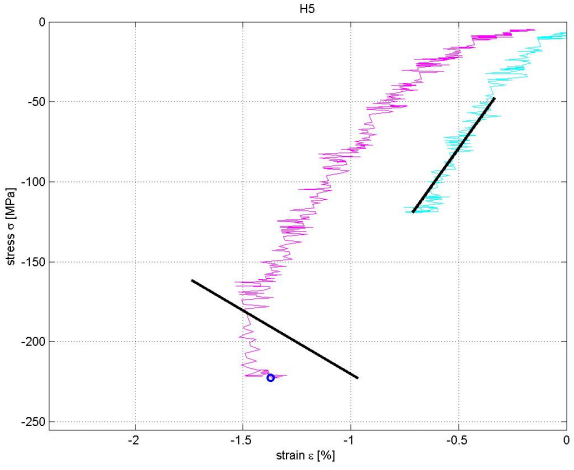

Figure 32: Unloading portions of stress-strain curves obtained from mechanical tests with maximum displacements of 0.048 mm and 0.097 mm for the sample with id K5. Black solid lines indicate linear fits computed as described in Subsection 2.2 of the Chapter 2; the blue circle depicts the ultimate stress and strain values

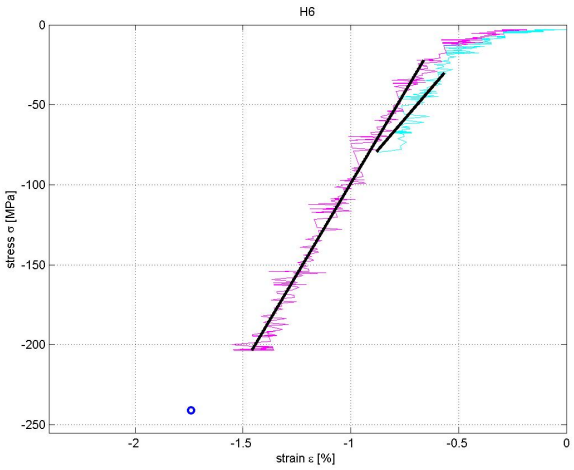

Figure 33: Unloading portions of stress-strain curves obtained from mechanical tests with maximum displacements of 0.048 mm and 0.097 mm for the sample with id K6. Black solid lines indicate linear fits computed as described in Subsection 2.2 of the Chapter 2; the blue circle depicts the ultimate stress and strain values

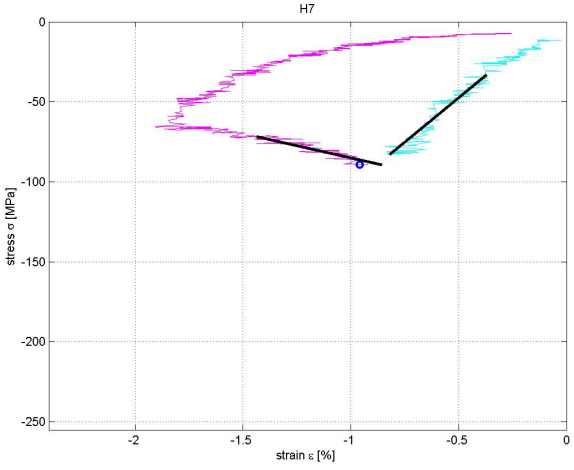

Figure 34: Unloading portions of stress-strain curves obtained from mechanical tests with maximum displacements of 0.048 mm and 0.097 mm for the sample with id K7. Black solid lines indicate linear fits computed as described in Subsection 2.2 of the Chapter 2; the blue circle depicts the ultimate stress and strain values

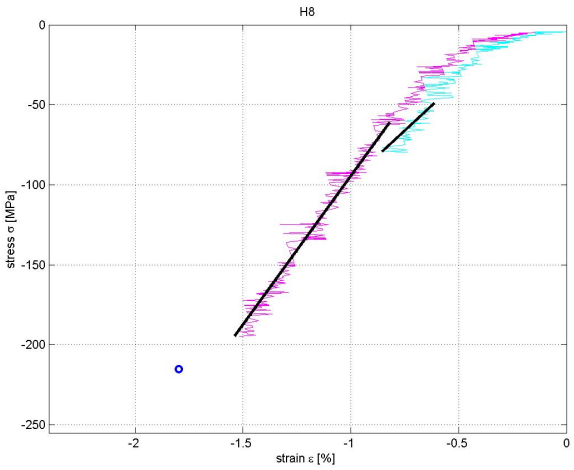

Figure 35: Unloading portions of stress-strain curves obtained from mechanical tests with maximum displacements of 0.048 mm and 0.097 mm for the sample with id K8. Black solid lines indicate linear fits computed as described in Subsection 2.2 of the Chapter 2; the blue circle depicts the ultimate stress and strain values

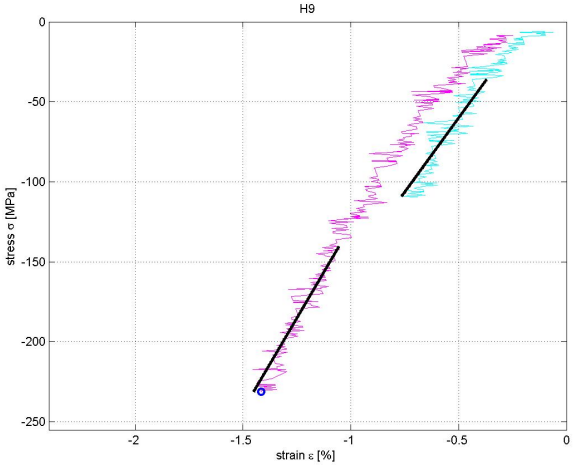

Figure 36: Unloading portions of stress-strain curves obtained from mechanical tests with maximum displacements of 0.048 mm and 0.097 mm for the sample with id K9. Black solid lines indicate linear fits computed as described in Subsection 2.2 of the Chapter 2; the blue circle depicts the ultimate stress and strain values

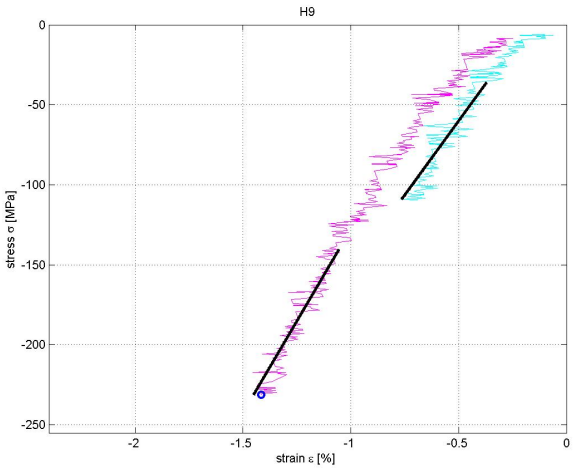

Figure 37: Unloading portions of stress-strain curves obtained from mechanical tests with maximum displacements of 0.048 mm and 0.097 mm for the sample with id K9. Black solid lines indicate linear fits computed as described in Subsection 2.2 of the Chapter 2; the blue circle depicts the ultimate stress and strain values

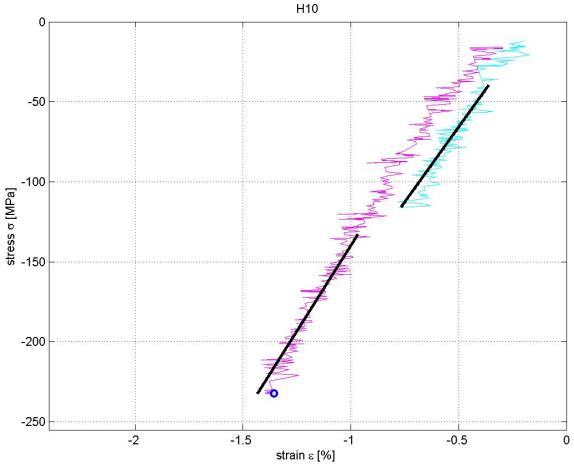

Figure 38: Unloading portions of stress-strain curves obtained from mechanical tests with maximum displacements of 0.048 mm and 0.097 mm for the sample with id K10. Black solid lines indicate linear fits computed as described in Subsection 2.2 of the Chapter 2; the blue circle depicts the ultimate stress and strain values

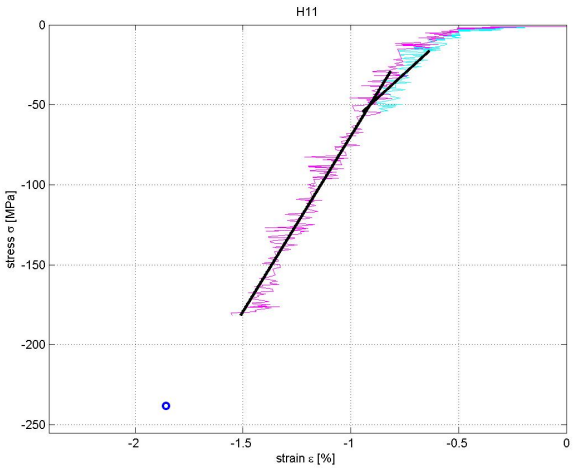

Figure 39: Unloading portions of stress-strain curves obtained from mechanical tests with maximum displacements of 0.048 mm and 0.097 mm for the sample with id K11. Black solid lines indicate linear fits computed as described in Subsection 2.2 of the Chapter 2; the blue circle depicts the ultimate stress and strain values

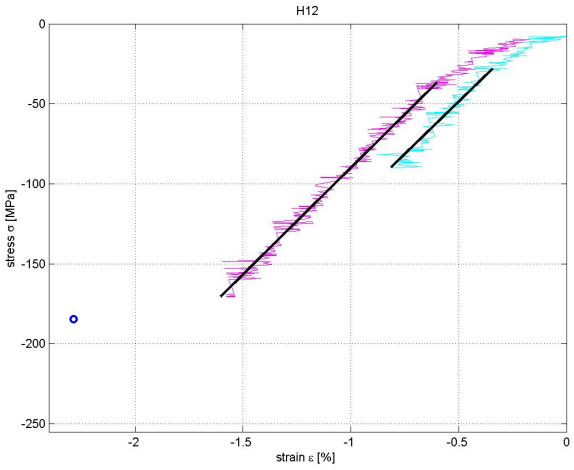

Figure 40: Unloading portions of stress-strain curves obtained from mechanical tests with maximum displacements of 0.048 mm and 0.097 mm for the sample with id K12. Black solid lines indicate linear fits computed as described in Subsection 2.2 of the Chapter 2; the blue circle depicts the ultimate stress and strain values

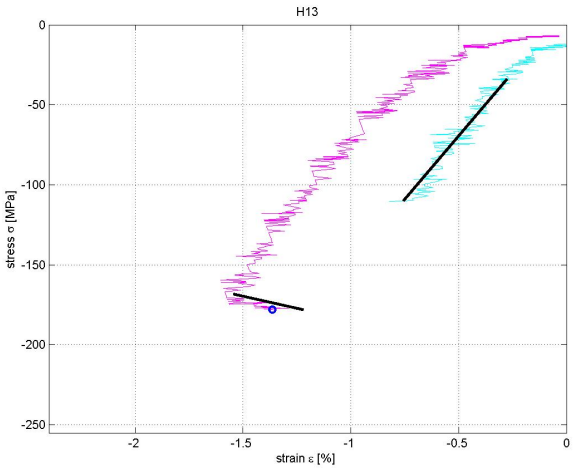

Figure 41: Unloading portions of stress-strain curves obtained from mechanical tests with maximum displacements of 0.048 mm and 0.097 mm for the sample with id K13. Black solid lines indicate linear fits computed as described in Subsection 2.2 of the Chapter 2; the blue circle depicts the ultimate stress and strain values

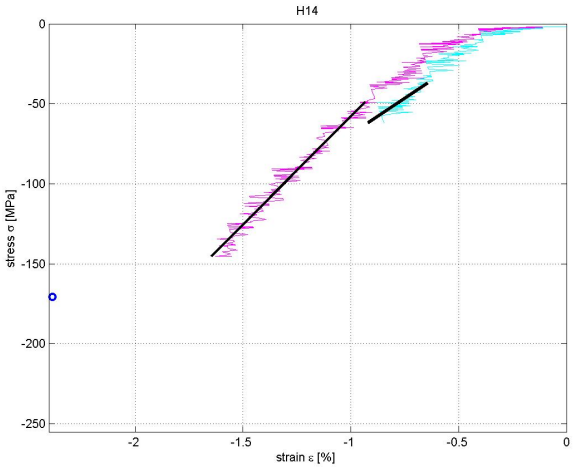

Figure 42: Unloading portions of stress-strain curves obtained from mechanical tests with maximum displacements of 0.048 mm and 0.097 mm for the sample with id K14. Black solid lines indicate linear fits computed as described in Subsection 2.2 of the Chapter 2; the blue circle depicts the ultimate stress and strain values

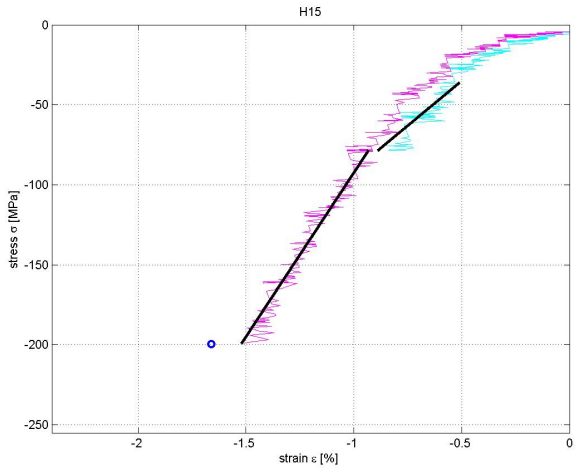

Figure 43: Unloading portions of stress-strain curves obtained from mechanical tests with maximum displacements of 0.048 mm and 0.097 mm for the sample with id K15. Black solid lines indicate linear fits computed as described in Subsection 2.2 of the Chapter 2; the blue circle depicts the ultimate stress and strain values

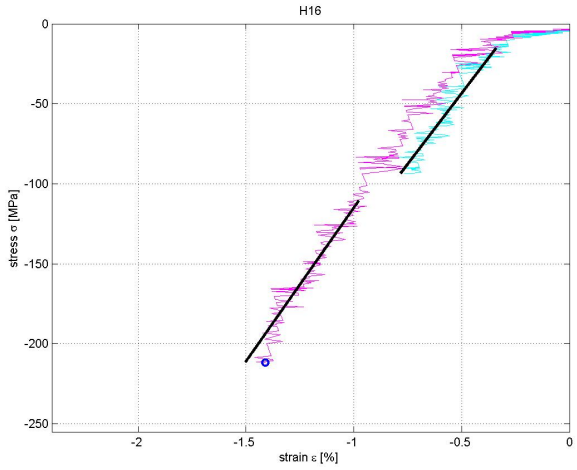

Figure 44: Unloading portions of stress-strain curves obtained from mechanical tests with maximum displacements of 0.048 mm and 0.097 mm for the sample with id K16. Black solid lines indicate linear fits computed as described in Subsection 2.2 of the Chapter 2; the blue circle depicts the ultimate stress and strain values

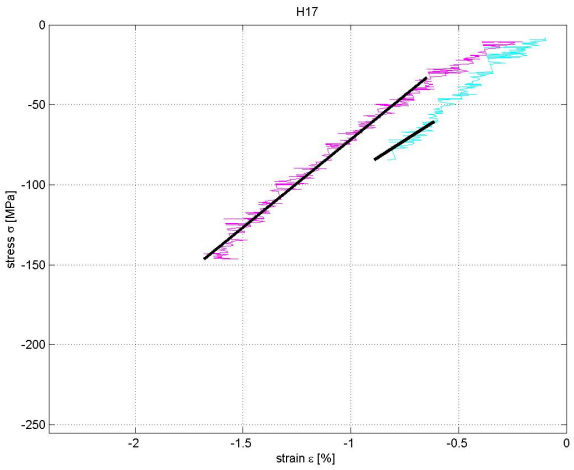

Figure 45: Unloading portions of stress-strain curves obtained from mechanical tests with maximum displacements of 0.048 mm and 0.097 mm for the sample with id K17. Black solid lines indicate linear fits computed as described in Subsection 2.2 of the Chapter 2; the blue circle depicts the ultimate stress and strain values

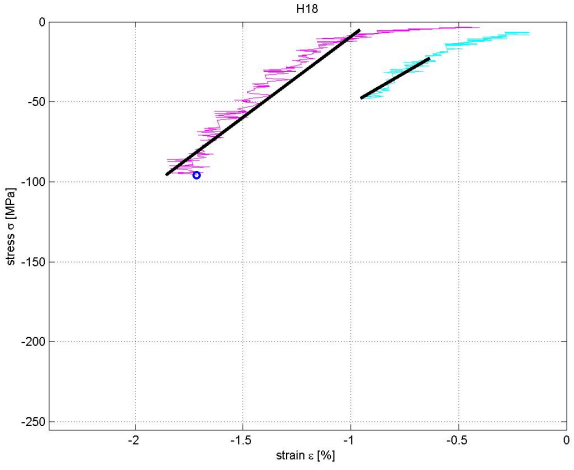

Figure 46: Unloading portions of stress-strain curves obtained from mechanical tests with maximum displacements of 0.048 mm and 0.097 mm for the sample with id K18. Black solid lines indicate linear fits computed as described in Subsection 2.2 of the Chapter 2; the blue circle depicts the ultimate stress and strain values

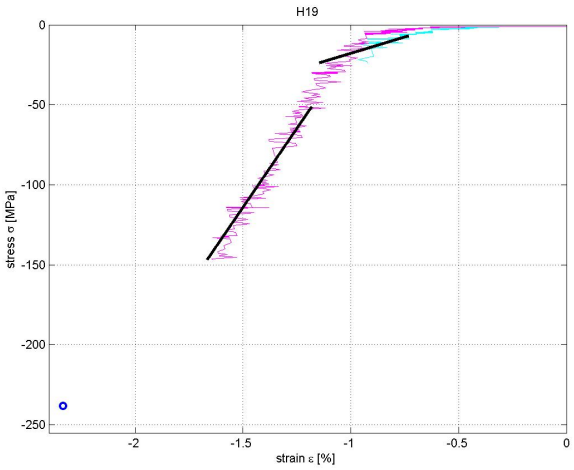

Figure 47: Unloading portions of stress-strain curves obtained from mechanical tests with maximum displacements of 0.048 mm and 0.097 mm for the sample with id K19. Black solid lines indicate linear fits computed as described in Subsection 2.2 of the Chapter 2; the blue circle depicts the ultimate stress and strain values

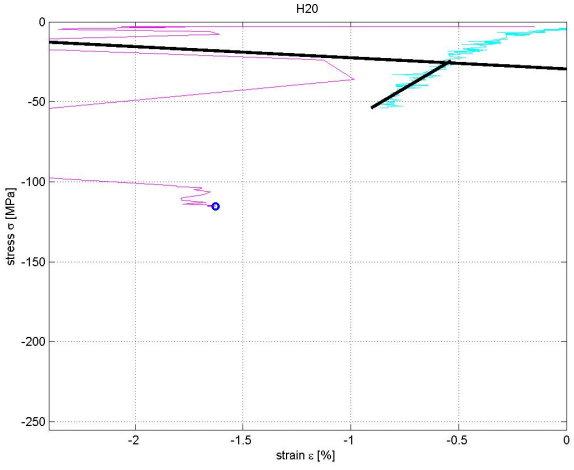

Figure 48: Unloading portions of stress-strain curves obtained from mechanical tests with maximum displacements of 0.048 mm and 0.097 mm for the sample with id K20. Black solid lines indicate linear fits computed as described in Subsection 2.2 of the Chapter 2; the blue circle depicts the ultimate stress and strain values

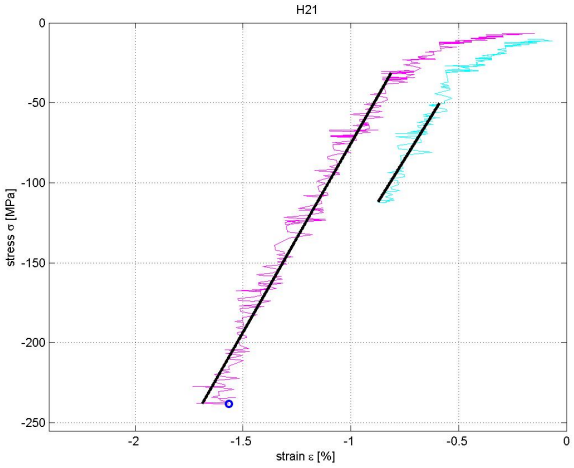

Figure 49: Unloading portions of stress-strain curves obtained from mechanical tests with maximum displacements of 0.048 mm and 0.097 mm for the sample with id K21. Black solid lines indicate linear fits computed as described in Subsection 2.2 of the Chapter 2; the blue circle depicts the ultimate stress and strain values

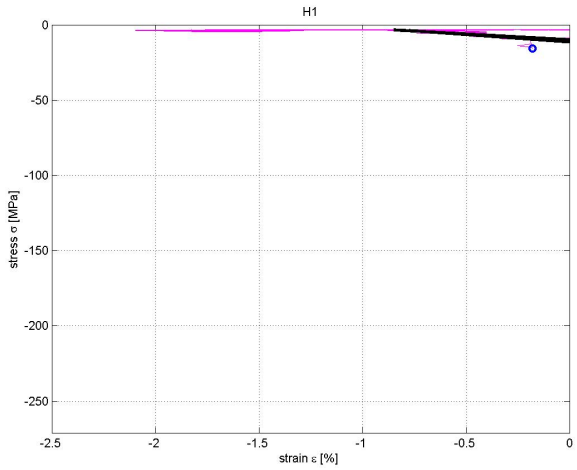

Figure 50: Unloading branches of a stress-strain characteristics stemming from mechanical tests, with a final displacements of 0.027 mm and 0.054 mm for the sample with id J1. Black solid lines indicate linear fits computed as described in subsection 2.2 of the Chapter 2; the blue circle depicts the ultimate stress and strain values

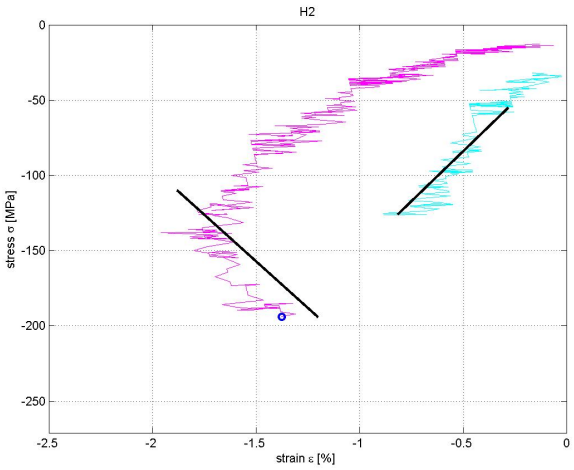

Figure 51: Unloading portions of stress-strain curves obtained from mechanical tests with maximum displacements of 0.027 mm and 0.054 mm for the sample with id J2. Black solid lines indicate linear fits computed as described in Subsection 2.2 of the Chapter 2; the blue circle depicts the ultimate stress and strain values

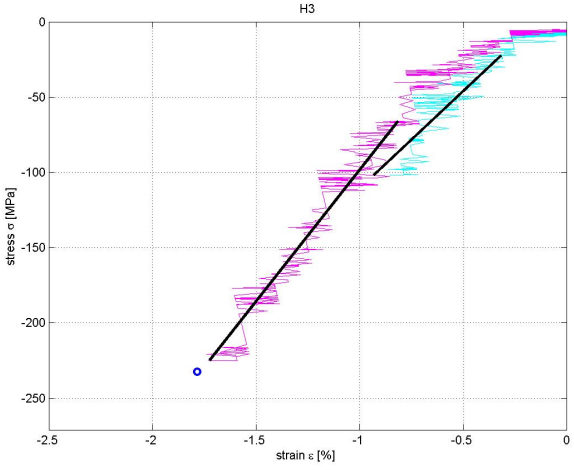

Figure 52: Unloading portions of stress-strain curves obtained from mechanical tests with maximum displacements of 0.027 mm and 0.054 mm for the sample with id J3. Black solid lines indicate linear fits computed as described in Subsection 2.2 of the Chapter 2; the blue circle depicts the ultimate stress and strain values

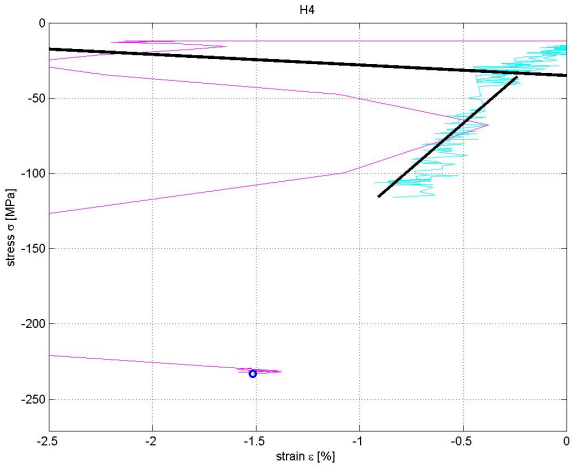

Figure 53: Unloading portions of stress-strain curves obtained from mechanical tests with maximum displacements of 0.027 mm and 0.054 mm for the sample with id J4. Black solid lines indicate linear fits computed as described in Subsection 2.2 of the Chapter 2; the blue circle depicts the ultimate stress and strain values

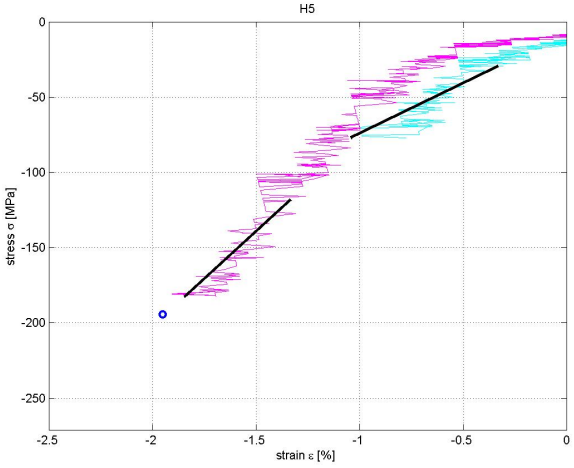

Figure 54: Unloading portions of stress-strain curves obtained from mechanical tests with maximum displacements of 0.027 mm and 0.054 mm for the sample with id J5. Black solid lines indicate linear fits computed as described in Subsection 2.2 of the Chapter 2; the blue circle depicts the ultimate stress and strain values

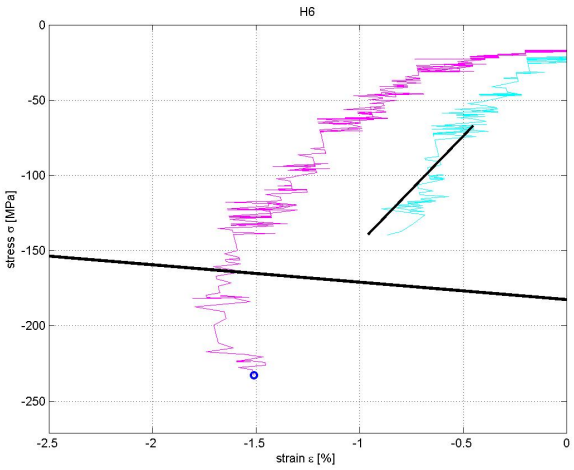

Figure 55: Unloading portions of stress-strain curves obtained from mechanical tests with maximum displacements of 0.027 mm and 0.054 mm for the sample with id J6. Black solid lines indicate linear fits computed as described in Subsection 2.2 of the Chapter 2; the blue circle depicts the ultimate stress and strain values

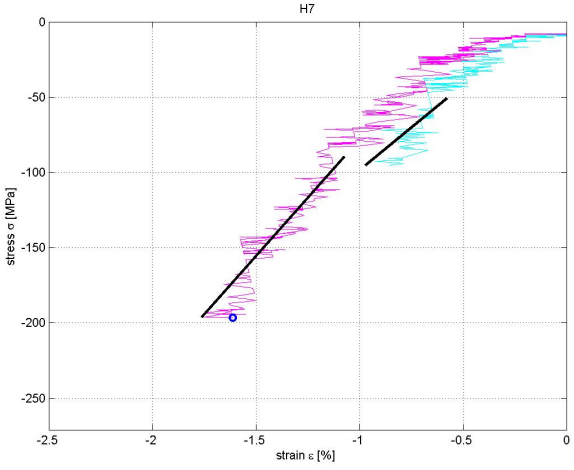

Figure 56: Unloading portions of stress-strain curves obtained from mechanical tests with maximum displacements of 0.027 mm and 0.054 mm for the sample with id J7. Black solid lines indicate linear fits computed as described in Subsection 2.2 of the Chapter 2; the blue circle depicts the ultimate stress and strain values

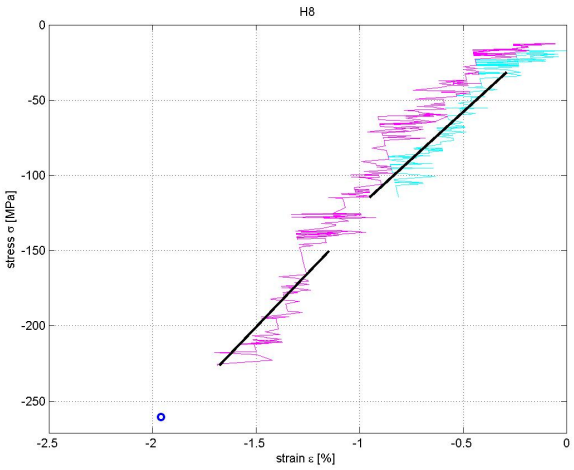

Figure 57: Unloading portions of stress-strain curves obtained from mechanical tests with maximum displacements of 0.027 mm and 0.054 mm for the sample with id J8. Black solid lines indicate linear fits computed as described in Subsection 2.2 of the Chapter 2; the blue circle depicts the ultimate stress and strain values

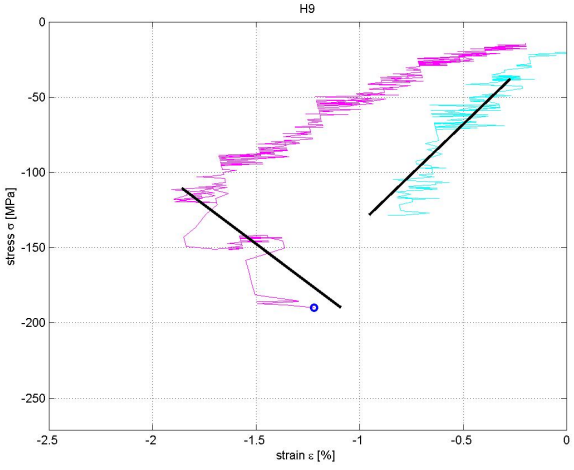

Figure 58: Unloading portions of stress-strain curves obtained from mechanical tests with maximum displacements of 0.027 mm and 0.054 mm for the sample with id J9. Black solid lines indicate linear fits computed as described in Subsection 2.2 of the Chapter 2; the blue circle depicts the ultimate stress and strain values

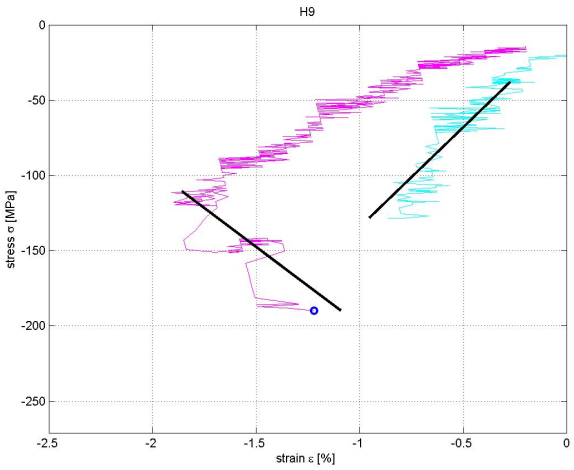

Figure 59: Unloading portions of stress-strain curves obtained from mechanical tests with maximum displacements of 0.027 mm and 0.054 mm for the sample with id J9. Black solid lines indicate linear fits computed as described in Subsection 2.2 of the Chapter 2; the blue circle depicts the ultimate stress and strain values

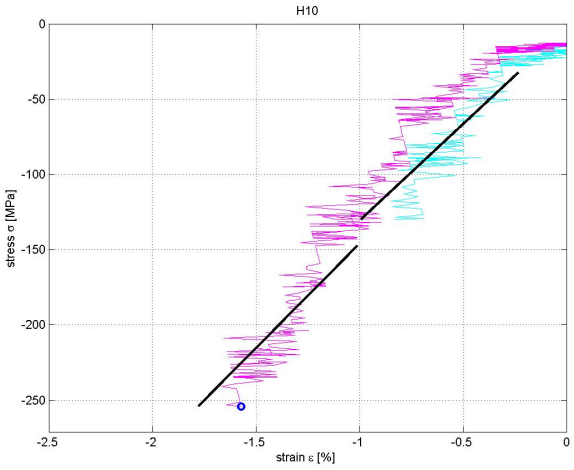

Figure 60: Unloading portions of stress-strain curves obtained from mechanical tests with maximum displacements of 0.027 mm and 0.054 mm for the sample with id J10. Black solid lines indicate linear fits computed as described in Subsection 2.2 of the Chapter 2; the blue circle depicts the ultimate stress and strain values

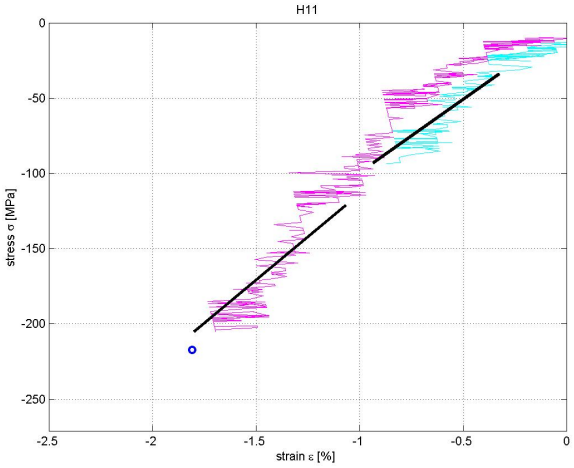

Figure 61: Unloading portions of stress-strain curves obtained from mechanical tests with maximum displacements of 0.027 mm and 0.054 mm for the sample with id J11. Black solid lines indicate linear fits computed as described in Subsection 2.2 of the Chapter 2; the blue circle depicts the ultimate stress and strain values

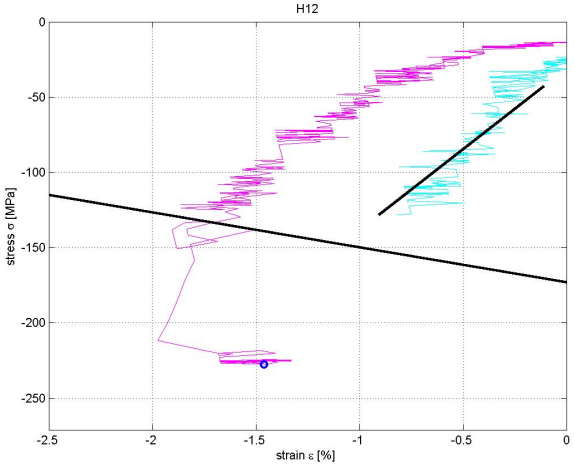

Figure 62: Unloading portions of stress-strain curves obtained from mechanical tests with maximum displacements of 0.027 mm and 0.054 mm for the sample with id J12. Black solid lines indicate linear fits computed as described in Subsection 2.2 of the Chapter 2; the blue circle depicts the ultimate stress and strain values

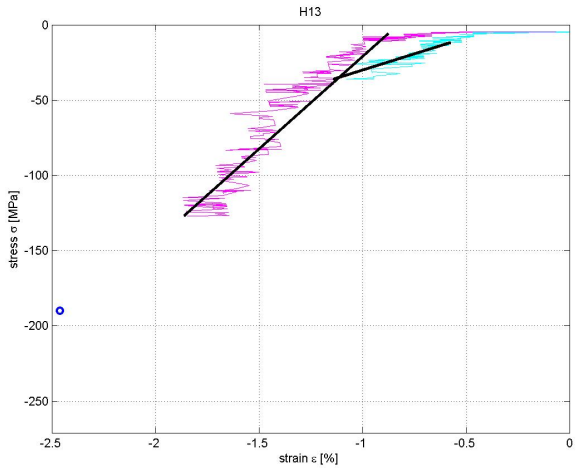

Figure 63: Unloading portions of stress-strain curves obtained from mechanical tests with maximum displacements of 0.027 mm and 0.054 mm for the sample with id J13. Black solid lines indicate linear fits computed as described in Subsection 2.2 of the Chapter 2; the blue circle depicts the ultimate stress and strain values

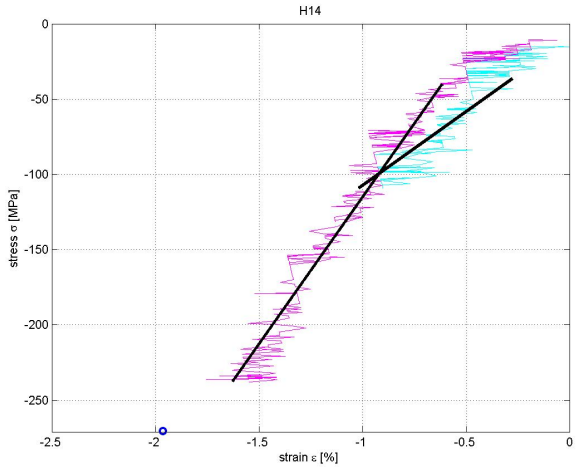

Figure 64: Unloading portions of stress-strain curves obtained from mechanical tests with maximum displacements of 0.027 mm and 0.054 mm for the sample with id J14. Black solid lines indicate linear fits computed as described in Subsection 2.2 of the Chapter 2; the blue circle depicts the ultimate stress and strain values

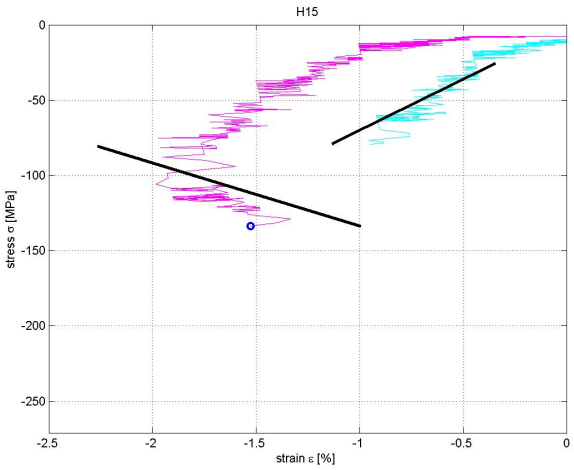

Figure 65: Unloading portions of stress-strain curves obtained from mechanical tests with maximum displacements of 0.027 mm and 0.054 mm for the sample with id J15. Black solid lines indicate linear fits computed as described in Subsection 2.2 of the Chapter 2; the blue circle depicts the ultimate stress and strain values

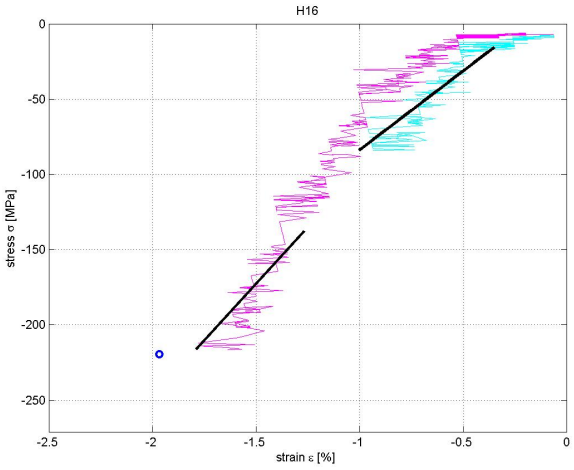

Figure 66: Unloading portions of stress-strain curves obtained from mechanical tests with maximum displacements of 0.027 mm and 0.054 mm for the sample with id J16. Black solid lines indicate linear fits computed as described in Subsection 2.2 of the Chapter 2; the blue circle depicts the ultimate stress and strain values

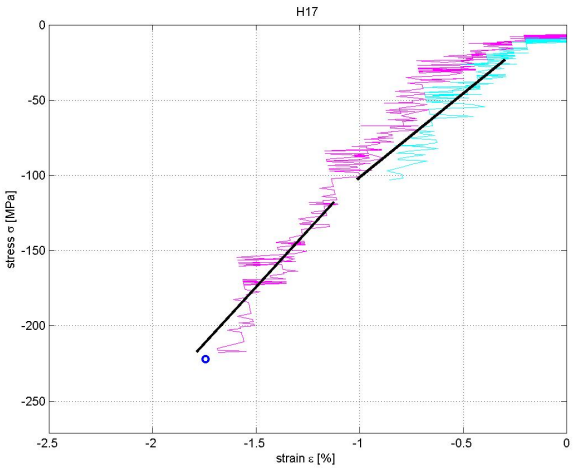

Figure 67: Unloading portions of stress-strain curves obtained from mechanical tests with maximum displacements of 0.027 mm and 0.054 mm for the sample with id J17. Black solid lines indicate linear fits computed as described in Subsection 2.2 of the Chapter 2; the blue circle depicts the ultimate stress and strain values

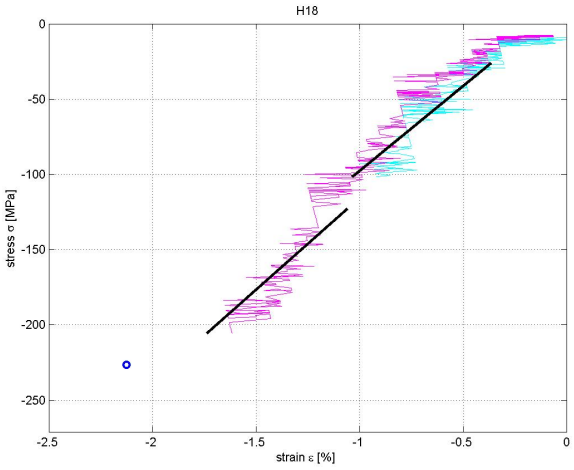

Figure 68: Unloading portions of stress-strain curves obtained from mechanical tests with maximum displacements of 0.027 mm and 0.054 mm for the sample with id J18. Black solid lines indicate linear fits computed as described in Subsection 2.2 of the Chapter 2; the blue circle depicts the ultimate stress and strain values

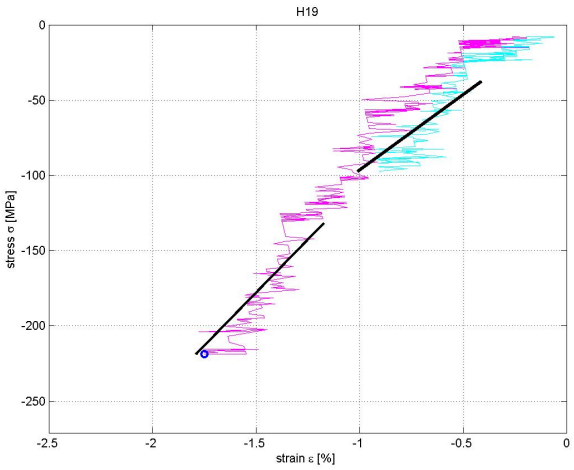

Figure 69: Unloading portions of stress-strain curves obtained from mechanical tests with maximum displacements of 0.027 mm and 0.054 mm for the sample with id J19. Black solid lines indicate linear fits computed as described in Subsection 2.2 of the Chapter 2; the blue circle depicts the ultimate stress and strain values

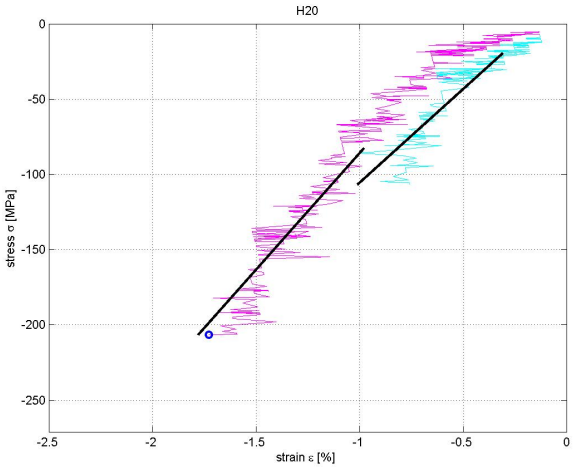

Figure 70: Unloading portions of stress-strain curves obtained from mechanical tests with maximum displacements of 0.027 mm and 0.054 mm for the sample with id J20. Black solid lines indicate linear fits computed as described in Subsection 2.2 of the Chapter 2; the blue circle depicts the ultimate stress and strain values

C Appendix III: Matlab source code used to derived the Young's moduli from the unloading branches of the stress-strain characteristics

```
clc; clear all;
d=[7.82 7.79 7.83 7.8 7.84 7.85 7.82 7.8 7.85
    7.82 7.83 7.85 7.83 7.82
    7.84 7.83 7.82 7.87 7.85 7.85 7.84 7.86]; %in mm
h=[12.76 12.47 12.86 12.38 12.52 12.68 12.67 12.55
    12.47 12.38 12.49 12.47 12.48 12.46 12.48 12.46 12.42
    12.49 12.43 12.53 12.43 12.56]; % in mm
sample=[12 13 14 15 16 17 18 19 20 21  22
    23 24 25 26 27 28 29 30 31 32];
preload=[30 50 50 130 60 40 30 30 50 50 70 30 30 60 20
    50 60 80 50 50 40 20]; %in N

sigma_stelle=zeros(length(sample),1);

start1=40;
start2=40;
for i=1:length(sample)
importfile(['raw_data/h',num2str(sample(i)),'.txt']);
Nachgiebigkeit=Kraft/71;
Kraft=Kraft+preload(i)/1000;%in KN
epsilon=(Weg-Nachgiebigkeit)/h(i)*100;
sigma=Kraft/((d(i))^2*pi/4)*10^3;
x_werte(:,i)=epsilon(1:1250);
y_werte(:,i)=sigma(1:1300);


%figure




sigma_max(i)=max(sigma);

sigma_stelle(i)=find(sigma==sigma_max(i));
epsilon_max(i)=epsilon(sigma_stelle(i));
```

```
[max1 pos1]=max(sigma(1:400));
[max2 pos2]=max(sigma(1:1200));

start_1(i)=pos1;
start_2(i)=pos2;



%linear Regession
SSxy1=0;
SSxx1=0;
SSyy1=0;
for k=20:150;
    steplength1=k;
    sigma_mean1=mean(sigma(pos1:pos1+steplength1));
    epsi_mean1=mean(epsilon(pos1:pos1+steplength1));
for j=1:length(sigma(pos1:pos1+steplength1));
    b=(sigma(j+pos1)-sigma_mean1)*(epsilon(j+pos1)-epsi_mean1);
    SSxy1=b+SSxy1;
   a=(epsilon(j+pos1)-epsi_mean1)^2;
   SSxx1=SSxx1+a;
   c=(sigma(j+pos1)-sigma_mean1)^2;
   SSyy1=SSyy1+c;



end
steig_EModul1=SSxy1/SSxx1/10;
   steig=sigma_mean1-steig_EModul1*10*epsi_mean1;
      y=sigma(pos1+steplength1);
      x=(y-steig)/steig_EModul1/10;
      rel=(x-epsilon(pos1+steplength1));
    e1_rel(i,k)=rel;
    e_rel(k)=rel;
    e1_mean(i,k)=mean(e_rel);
    e1_std(i,k)=std(e_rel);
    if k==150;
        e_rel=0;
    end
```

```
    s_mean1(i,k)=sigma_mean1;
    e_mean1(i,k)=epsi_mean1;
   Reg_EModul1(i,k)=SSxy1/SSxx1/10;
    R2_1(i,k)=SSxy1^2/(SSxx1*SSyy1);

end


SSxy2=0;
SSxx2=0;
SSyy2=0;
for k=20:300;
    steplength2=k;
    sigma_mean2=mean(sigma(pos2:pos2+steplength2));
    epsi_mean2=mean(epsilon(pos2:pos2+steplength2));

for j=1:length(sigma(pos2:pos2+steplength2));
    b=(sigma(j+pos2)-sigma_mean2)*(epsilon(j+pos2)-epsi_mean2);
    SSxy2=b+SSxy2;
   a=(epsilon(j+pos2)-epsi_mean2)^2;
   SSxx2=SSxx2+a;
   c=(sigma(j+pos2)-sigma_mean2)^2;
   SSyy2=SSyy2+c;



end
        steig_EModul2=SSxy2/SSxx2/10;
   steig=sigma_mean2-steig_EModul2*10*epsi_mean2;
      y=sigma(pos2+steplength2);
      x=(y-steig)/steig_EModul2/10;
      rel=(x-epsilon(pos2+steplength2));
    e2_rel(i,k)=rel;
    e_rel(k)=rel;
    e2_mean(i,k)=mean(e_rel);
    e2_std(i,k)=std(e_rel);
    if k==300
        e_rel=0;
    end
```

```
 s_mean2(i,k)=sigma_mean2;
     e_mean2(i,k)=epsi_mean2;
R2_2(i,k)=SSxy2^2/(SSxx2*SSyy2);
Reg_EModul2(i,k)=SSxy2/SSxx2/10;
end

end
R2_1(:,~any(R2_1))=[];
R2_2(:,~any(R2_2))=[];
e_mean1(:,~any(e_mean1))=[];
s_mean1(:,~any(s_mean1))=[];
e_mean2(:,~any(e_mean2))=[];
s_mean2(:,~any(s_mean2))=[];
e1_std(:,~any(e1_std))=[];
e2_std(:,~any(e2_std))=[];


[e_1_std, b1] = min( e1_std(1:end,(start1+1):end), [], 2 );
[e_2_std, b2] = min( e2_std(1:end,(start2+1):end), [], 2 );
Reg_EModul1(:,~any(Reg_EModul1))=[];
[R2_1max, b1notused] = max( R2_1, [], 2 );
Reg_EModul2(:,~any(Reg_EModul2))=[];
[R2_2max, b2notused] = max( R2_2, [], 2 );




R2_1= transpose(R2_1);
R2_2= transpose(R2_2);

Reg_EModul1=transpose(Reg_EModul1);
Reg_EModul2=transpose(Reg_EModul2);


s_mean1=transpose(s_mean1);
e_mean1=transpose(e_mean1);
 s_mean2=transpose(s_mean2);
e_mean2=transpose(e_mean2);
```

```
z1=0;
z2=0;
for n=1:length(sample);

   j1=b1(n)+z1+start1;
   x1(n)=e_mean1(j1);
   y1(n)=s_mean1(j1);
   R2_a(n)=R2_1(j1);
   EModul1(n)=Reg_EModul1(j1);

   z1=j1+length(R2_1)-b1(n)-start1;


   j2=b2(n)+z2+start2;
    x2(n)=e_mean2(j2);
   y2(n)=s_mean2(j2);
   R2_b(n)=R2_2(j2);
    EModul2(n)=Reg_EModul2(j2);
   z2=j2+length(R2_2)-b2(n)-start2;

   a1(n)=y1(n)-EModul1(n)*10*x1(n);
   y_1=y_werte(start_1(n),n):-1/100:
   y_werte(start_1(n)+b1(n)+start1,n);
   x_1=(y_1-a1(n))/EModul1(n)/10;

      a2(n)=y2(n)-EModul2(n)*10*x2(n);
   y_2=y_werte(start_2(n),n):-1/100:
   y_werte(start_2(n)+b2(n)+start2,n);
   x_2=(y_2-a2(n))/EModul2(n)/10;

   figure


   plot(-x_werte(start_1(n):398,n),-y_werte(start_1(n):398,n),'c',
   -x_werte(start_2(n):1198,n),-y_werte(start_2(n):1198,n)
   ,'m','linewidth',0.7)
   hold on
   plot(-epsilon_max(n),-sigma_max(n),'o','linewidth',2)

   plot(-x_1,-y_1,'color','k','linewidth',2.5)
```

```
  plot(-x_2,-y_2,'color','k','linewidth',2.5)
  %Plot Export
      grid on
ylabel('stress \sigma [MPa]')
xlabel('strain \epsilon [%] ')

title(['H',num2str(sample(n))]);
% set(gca,'xdir','reverse');
% set(gca,'ydir','reverse');
xlim([-2.4 0])
ylim([-225 0])
hold on
saveas( gcf,['pic/H',num2str(sample(n))], 'jpg' );
%       exportfig(gcf,['img/',num2str(sample(n)),'.eps'], ...
%     'width',6, 'fontmode','fixed',...
%     'color','cmyk', 'fontsize',13, 'LineWidth', 3);


      close all

      e_1(n)=x_werte(start_1(n));
      e_2(n)=x_werte(start_2(n));
    end

e_1=transpose(e_1);
e_2=transpose(e_2);
EModul1=transpose(EModul1);
EModul2=transpose(EModul2);



sample= transpose(sample);
sigma_max=transpose(sigma_max);
epsilon_max=transpose(epsilon_max);
%z =[sample EModul1  EModul2 sigma_max epsilon_max e_1 e_2]
z=EModul1
z=EModul2
```

References

[Fritsch et al., 2009] Fritsch, A., Hellmich, C., and Dormieux, L. (2009). Ductile sliding between mineral crystals followed by rupture of collagen crosslinks: experimentally supported micromechanical explanation of bone strength. *Journal of Theoretical Biology*, 260(2):230–252.

[Lees et al., 1979] Lees, S., Heeley, J. D., and Cleary, P. F. (1979). A study of some properties of a sample of bovine cortical bone using ultrasound. *Calcified Tissue International*, 29(1):107–117.

[Luczynski et al., 2013] Luczynski, K. W., Brynk, T., Ostrowska, B., Swieszkowski, W., Reihsner, R., and Hellmich, C. (2013). Consistent quasistatic and acoustic elasticity determination of poly-l-lactide-based rapid-prototyped tissue engineering scaffolds. *Journal of Biomedical Materials Research Part A*, 101(1):138–144.

[Morin and Hellmich, 2014] Morin, C. and Hellmich, C. (2014). A multiscale poromicromechanical approach to wave propagation and attenuation in bone. *Ultrasonics*.

[Salençon, 2001] Salençon, J. (2001). *Handbook of continuum mechanics: general concepts-thermoelasticity*. Springer.

[Turner and Burr, 1993] Turner, C. H. and Burr, D. B. (1993). Basic biomechanical measurements of bone: a tutorial. *Bone*, 14(4):595–608.